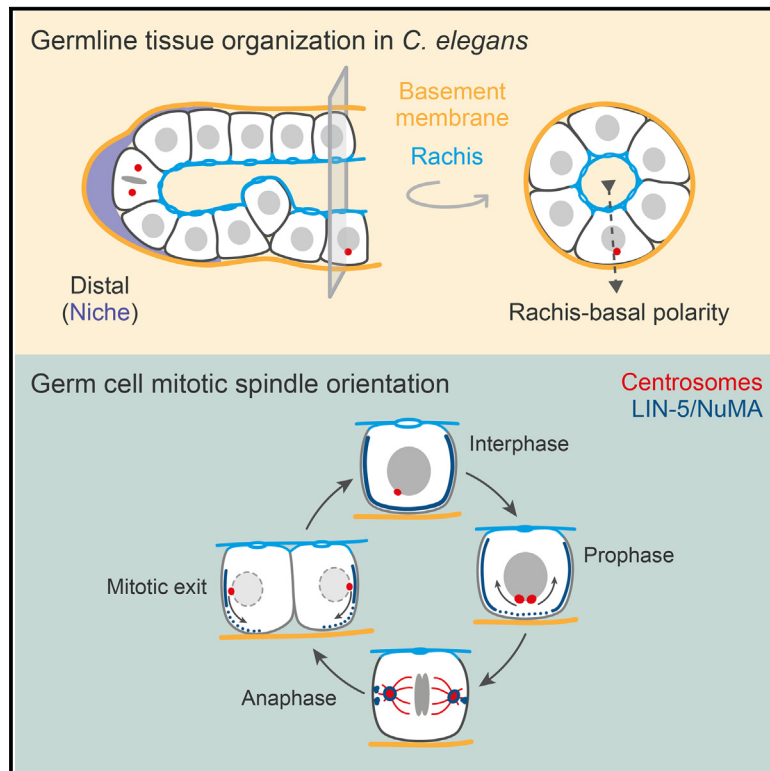


The spatiotemporal distribution of LIN-5/NuMA regulates spindle orientation in the *C. elegans* germ line

Graphical abstract



Authors

Réda M. Zellag, Vincent Poupart, Takefumi Negishi, Jean-Claude Labbé, Abigail R. Gerhold

Correspondence

jc.labbe@umontreal.ca (J.-C.L.),
abigail.gerhold@mcgill.ca (A.R.G.)

In brief

Zellag et al. use *in situ* live-cell imaging to show that mitotic spindles orient parallel to the tissue plane in the *C. elegans* germ line. They propose a mechanism wherein basal centrosome positioning in interphase and a cycle of LIN-5/NuMA cortical localization establishes and maintains proper germ cell spindle orientation during mitosis.

Highlights

- Mitotic spindles orient parallel to the tissue plane in the *C. elegans* germ line
- Spindle orientation is set up in prophase and actively maintained through anaphase
- Proper spindle orientation depends upon LIN-5/NuMA and dynein
- Interphase centrosome position and LIN-5/NuMA cortical dynamics predict spindle orientation



Article

The spatiotemporal distribution of LIN-5/NuMA regulates spindle orientation in the *C. elegans* germ line

Réda M. Zellag,^{1,2,3} Vincent Poupart,¹ Takefumi Negishi,^{4,5} Jean-Claude Labbé,^{1,2,*} and Abigail R. Gerhold^{3,6,*}¹Institute for Research in Immunology and Cancer (IRIC), Montréal, QC H3C 3J7, Canada²Department of Pathology and Cell Biology, Université de Montréal, C.P. 6128, Succ. Centre-ville, Montréal, QC H3C 3J7, Canada³Department of Biology, McGill University, 1205 Avenue Docteur Penfield, Montréal, QC H2A 1B1, Canada⁴Multicellular Organization Laboratory, Department of Gene Function and Phenomics, National Institute of Genetics, Research Organization of Information and Systems (ROIS), Mishima, Shizuoka 411-8540, Japan⁵Department of Genetics, School of Life Sciences, SOKENDAI (The Graduate University for Advanced Studies), Mishima, Shizuoka 411-8540, Japan⁶Lead contact*Correspondence: jc.labbe@umontreal.ca (J.-C.L.), abigail.gerhold@mcgill.ca (A.R.G.)<https://doi.org/10.1016/j.celrep.2025.115296>

SUMMARY

Mitotic spindle orientation contributes to tissue organization and shape by setting the cell division plane. How spindle orientation is coupled to diverse tissue architectures is incompletely understood. The *C. elegans* gonad is a tube-shaped organ with germ cells forming a circumferential monolayer around a common cytoplasmic lumen. How this organization is maintained during development is unclear, as germ cells lack the canonical cell-cell junctions that ensure spindle orientation in other tissue types. Here, we show that the microtubule force generator dynein and its conserved regulator LIN-5/NuMA regulate germ cell spindle orientation and are required for germline tissue organization. We uncover a cyclic, polarized pattern of LIN-5/NuMA cortical localization that predicts centrosome positioning throughout the cell cycle, providing a means to align spindle orientation with the tissue plane. This work reveals a new mechanism by which oriented cell division can be achieved to maintain tissue organization during animal development.

INTRODUCTION

The ability of organs to perform specialized functions such as nutrient absorption or reproduction depends upon the development of proper tissue architecture. This requires the coordination of cell behavior, including the orientation of cell division, which, by determining the position of daughter cells, can impact both tissue shape and organization.^{1,2} Oriented cell division relies on cortical force generators, typically the molecular motor protein dynein and its activator nuclear mitotic apparatus (NuMA), which act on astral microtubules to position the mitotic spindle and thereby dictate the axis of cell division.³

Several mechanisms have been described by which the activity and/or localization of cortical force generators are regulated to generate oriented cell divisions. For example, spindles in epithelial cells are typically oriented perpendicular to the apical-basal cell axis, and thus parallel to the plane of the tissue, and can be influenced by tissue-scale tension or patterning to provide an additional orientation bias within the tissue plane (so-called planar orientation). Apical-basal orientation involves concentrating the force-generating machinery along lateral cell cortices^{4,5} by coupling its localization to apical-basal polarity and/or cell-cell junctional cues.^{6–12} Planar orientation has

been linked to the often interdependent phenomena of tissue tension,^{13–18} cell shape,^{16–22} and planar cell polarity.^{1,23–25} In most cases, planar orientation is also dictated by the association of cortical force generators with cell junctions (e.g., tri-cellular junctions^{20,21}) and/or cell adhesion proteins (e.g., cadherins¹⁵). However, several exceptions have been noted,^{13,15} and examples of novel mechanisms are still emerging (e.g., Negishi et al.²⁶). Thus, a full picture of the diversity of mechanisms regulating spindle orientation during development is lacking.

The *C. elegans* gonad is a well-established model for the study of germline tissue development, yet relatively little is known about how germ cell spindle orientation is regulated. In adult hermaphrodites, the gonad forms two symmetric U-shaped arms, each capped at its distal end by a distal tip cell (DTC) that serves as a niche for the underlying mitotic germ cells.^{27,28} Within each gonad arm, germ cells are arranged in a rough circumferential monolayer around a common, central core of cytoplasm called the rachis (Figure 1A; see also Hirsh et al.²⁹ and Hall et al.³⁰). Each germ cell is connected to the rachis via a single cytoplasmic bridge that is maintained by a stable actomyosin ring, polarizing germ cells along their rachis-basal axis and forming a tissue-scale, tensile actomyosin network at the rachis surface.^{30–33} Germ cell cytoplasmic bridges constrict in mitosis, but rachis markers remain



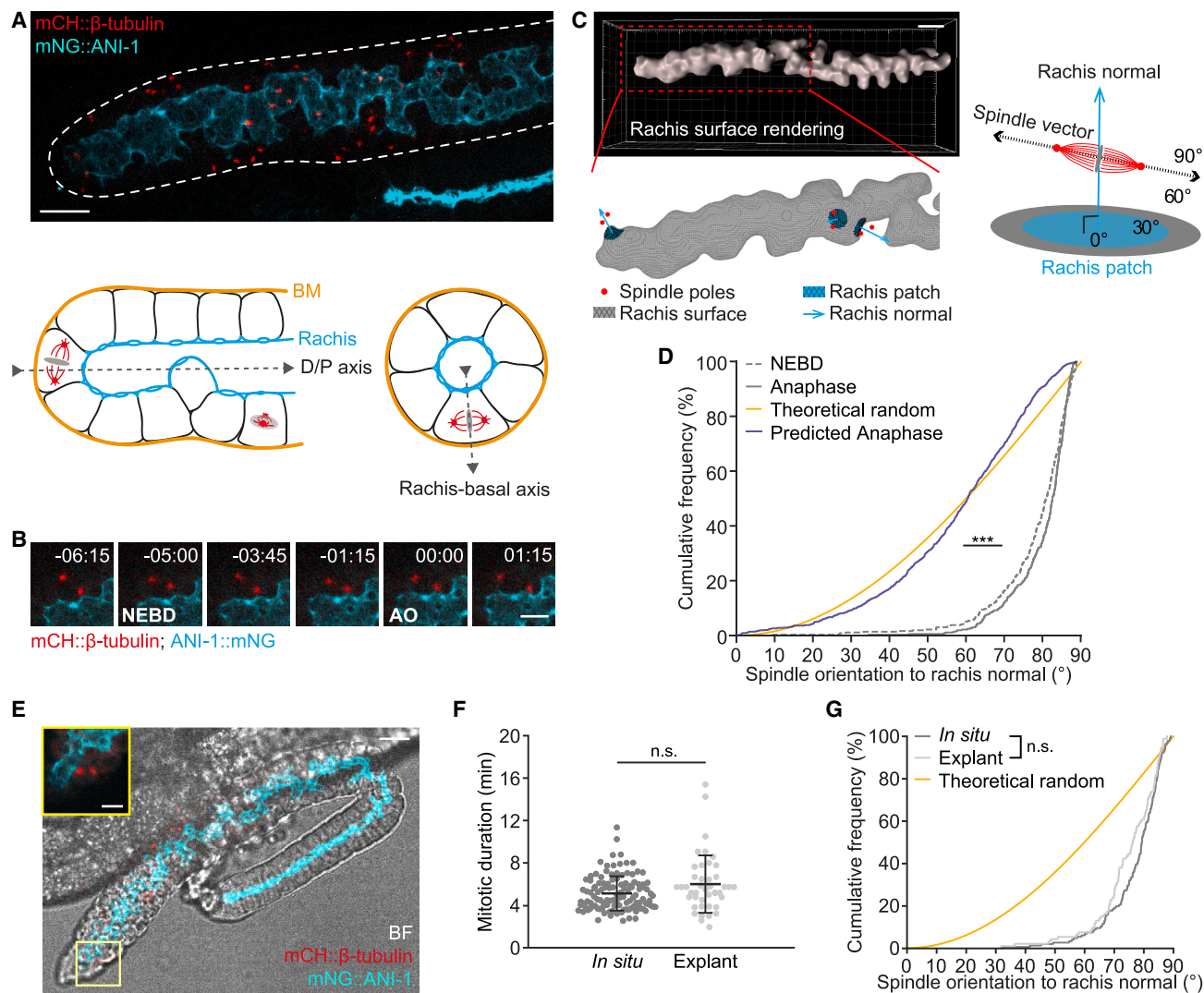


Figure 1. Germ cell spindles orient parallel to the rachis surface *in situ* and in gonad explants

(A) Top: maximum-intensity projection of a gonad arm from an L4 larva expressing mCH::β-tubulin (red) in the germ line and endogenously tagged mNG::ANI-1 (cyan) to mark spindle poles and the rachis, respectively. Scale bar, 10 μm. Bottom: schematic representations of a distal gonad arm viewed length-wise (left) and en face (right). BM, basement membrane; D/P, distal/proximal.

(B) Maximum-intensity projections of a germ cell, expressing mCH::β-tubulin (red) and mNG::ANI-1 (cyan), undergoing mitosis. Numbers indicate time in minutes relative to anaphase onset. NEBD, nuclear envelope breakdown; AO, anaphase onset. Scale bar, 5 μm.

(C) Representative rachis surface rendering from the mNG::ANI-1 signal (top) with a reconstruction of the rachis surface, showing a subset of mitotic spindles in relation to their respective rachis surface patches and rachis normal vectors (bottom). Scale bar, 10 μm. A schematic depicting spindle orientation to the rachis surface as the angle formed between the spindle vector and rachis normal is shown on the right.

(D) Cumulative distribution of spindle angles to the rachis normal for germ cells in L4 larvae at NEBD and anaphase as compared to the theoretical random (yellow) and predicted anaphase (purple) distributions.

(E) Bright-field image of a gonad explant from an L4 larva overlaid with a maximum-intensity projection of mNG::ANI-1 (cyan) and mCH::β-tubulin (red). Scale bar, 10 μm. Inset shows a mitotic germ cell. Scale bar, 5 μm

(F) The duration of germ cell mitosis *in situ* and in gonad explants. Bars indicate the mean ± standard deviation.

(G) Cumulative distribution of spindle angles to the rachis normal for measurements made at anaphase *in situ* and in explants, with the theoretical random distribution shown for comparison. *In situ* data were drawn at random from the dataset used in Figure S1B.

For all panels, n.s. $p > 0.05$; *** $p < 0.001$. Summary statistics and statistical tests used are given in Table S3. See also Figures S1 and S2 and Video S1.

enriched on their rachis face (Figure 1B; see Seidel et al.³⁴). This architecture is present throughout development,^{31,35} as the number of germ cells increases from two primordial germ cells in newly hatched L1 larvae to ~2,000 germ cells in adults^{27,28} and as each

gonad arm elongates along its distal/proximal (D/P) axis, undergoing a 180° turn to attain its final U-like shape.^{27,36}

C. elegans germ cells, like epithelial cells, are thought to divide within the plane of the germline tissue (Figures 1A and 1B; see

Seidel et al.³⁴). They also exhibit a mild orientation bias relative to the gonadal D/P axis.³⁷ The former could serve to maintain the germline monolayer and ensure that each daughter cell remains connected to the rachis after cell division, while the latter could contribute to, or arise from, the elongated gonad tissue shape. However, the mechanisms aligning germ cell spindles to either axis are unknown, and the functional consequences of disrupting spindle orientation have not been assessed. Moreover, *C. elegans* germ cells lack cell-cell junctions^{29,30} and must therefore rely on other means for orienting cell division.

Here, we use live-cell imaging of *C. elegans* germ cells *in situ* and in gonad explants to investigate the regulation of spindle orientation during gonad development. Our results support a model wherein the exclusion of LIN-5/NuMA from the germ cell rachis surface throughout the cell cycle, coupled with the basal localization of centrosomes during interphase, establishes spindle orientation parallel to the rachis surface during prophase. The dynamic association of LIN-5/NuMA with lateral cortices adjacent to spindle poles during mitosis then maintains this orientation into anaphase, thus positioning both daughter cells in the plane of the tissue.

RESULTS

Mitotic spindles are oriented parallel to the rachis surface in *C. elegans* germ cells

To assess spindle orientation in dividing *C. elegans* germ cells, we developed an approach to identify the rachis surface for each cell and to measure spindle orientation relative to this surface through time. This task was complicated by the fact that the rachis core is tortuous³⁴ and that germ cells can divide within the 3D tube-like structure of the gonad at any angle relative to the imaging plane (see [Figures 1A and 1B](#) and [Video S1](#)). We used animals that express fluorescent protein (FP)-tagged versions of β -tubulin to track and pair centrosomes^{37,38} and the actomyosin scaffold protein anillin (ANI-1^{31,39}) to generate a 3D rendering of the rachis surface ([Figure 1C](#)). We then identified the rachis patch nearest to each mitotic spindle and represented its orientation as the normal vector to the rendered surface (hereafter the rachis normal). Spindle orientation in relation to the rachis surface was then defined as the angle formed between the spindle vector and the rachis normal vector in 3D ([Figure 1C](#); see [STAR Methods](#)). Accordingly, spindles perfectly parallel to their relevant rachis surface will be orthogonal to the rachis normal, with a spindle angle of 90°. Measurements were done on L4 larvae, a developmental stage characterized by robust germ cell proliferation and sustained gonad growth.^{27,28}

We found that the majority of germ cell spindles are roughly orthogonal to the rachis normal in anaphase (and thus parallel to the rachis surface), with 98% of spindles having an angle of 60° or greater ([Figure 1D](#)). We calculated the theoretical range of angles that spindles could assume during anaphase elongation without forcing spindle poles into contact with the rachis surface plane (see [STAR Methods](#)) and found a good concordance with our measured values—in theory, an angle of 53° or greater, relative to the rachis normal, should prevent spindle poles from contacting the rachis surface and, across all cells, only two of 503 spindles had a measured angle less than this value

([Figures S1A and S1B](#)). Thus, the range of spindle angles that we observe is consistent with a relative lack of spindle pole engagement with the rachis surface.

We also found that spindles were already oriented parallel to the rachis surface at nuclear envelope breakdown (NEBD) ([Figure 1D](#)). We considered the possibility that a bias in spindle orientation at NEBD would be sufficient to ensure that spindles maintain this orientation into anaphase. We measured the magnitude of spindle rotations relative to the rachis normal during prometa/metaphase and used this to predict spindle orientation at anaphase onset if no constraints were placed on the direction of rotation ([Figures S1C and S1D](#)). We found that spindle orientation in anaphase would be considerably more variable if spindles rotated freely ([Figures 1D and S1C–S1D](#)). Thus, we infer that spindle rotations during prometa/metaphase tend to be oscillatory, and that an active mechanism is required to maintain spindle orientation parallel to the rachis surface through anaphase.

Germ cell spindles orient parallel to the rachis surface irrespective of developmental stage and distance to the niche

We next assessed whether spindle orientation was influenced by developmental changes in tissue organization. As animals progress from the L4 larval stage into adulthood, the rachis becomes increasingly tortuous, with the germ line adopting a folded organization ([Figure S1E](#); see Seidel et al.³⁴). However, germ cell spindles were oriented parallel to the rachis surface in anaphase both in L3 larvae, when the germ line lacks folds, and in 1-day-old adults, in which germ line folds are more pronounced ([Figure S1F](#)).

We also considered whether germ cell position along the gonadal D/P axis, and thus distance from the niche, affected spindle orientation to the rachis surface ([Figure S1G](#)). However, the same anaphase spindle orientation bias was present from the distal-most region of the gonad to the mitotic-to-meiotic transition zone ([Figure S1H](#)). Together, these results indicate that spindle orientation relative to the rachis surface is robust to changes in germline organization during development and germ cell differentiation as cells exit the niche.

Spindle orientation in germ cells is gonad autonomous

The gonad in L4 larvae consists of the germ line and somatic gonadal cells, including the DTC niche and the gonadal sheath cells, which enwrap each gonad arm, and the entire organ is radially constrained by the shape of the animal and adjacent tissues.²⁷ To determine whether spindle orientation in germ cells is influenced by mechanical constraints external to the gonad, we tracked germ cell divisions in gonad explants. We extruded gonads into a medium permissible for *C. elegans* embryonic blastomere culture⁴⁰ ([Figure 1E](#); see [STAR Methods](#)). Following extrusion, explants retained somatic gonadal cells and the gonadal basement membrane ([Figures S2A and S2B](#)) and maintained proper germline architecture ([Figure 1E](#)), suggesting that they are largely intact. We found that mitotic duration and the rate of spindle elongation in germ cells dividing in explants were similar to those measured *in situ* ([Figures 1F and S2C](#)), indicating that germ cell physiology was relatively normal. Notably,

as in germ cells dividing *in situ*, spindle orientation in germ cells dividing in explants was strongly biased parallel to the surface of the rachis (Figure 1G). Gonad explants also showed a spindle orientation bias relative to the gonadal D/P axis (Figure S2D), as we previously observed *in situ*.³⁷ These results indicate that spindle orientation in germ cells is independent of constraints imposed by other anatomical features of the animal and that the mechanisms regulating spindle orientation are autonomous to the gonad tissue.

Spindle orientation to the rachis surface occurs independently of cell shape

In many cell types, the cell's long axis predicts the orientation of division (the so-called long-axis rule, as proposed by Hertwig^{41, 17, 19, 20, 22, 42, 43} although exceptions have been noted.^{13–15} Thus, spindle orientation in germ cells could be a consequence of germ cell shape. To address this possibility, we assessed germ cell shape in mitotic and interphase cells using animals in which centrosomes (β -tubulin), the rachis surface (either ANI-1 or the septin UNC-59^{37, 44}), and the plasma membrane (the PH domain of rat PLC1 δ ^{45, 46}) were marked (Figure 2A). Rendering of the membrane marker in 3D allowed us to fit an ellipsoid to each germ cell and determine the length and orientation of the cell's major (i.e., long) and minor axes. We found that germ cells were mildly anisotropic, with mitotic cells being on average larger and more spherical than the largest interphase cells (Figures 2B and 2C), consistent with cell growth occurring prior to mitotic entry and mitotic cell rounding.

To determine whether the interphase cell long axis predicts spindle orientation in anaphase, we measured its orientation to the rachis normal. We found that the interphase cell long axis could adopt roughly any orientation with respect to the rachis normal (Figure 2D), suggesting that germ cells, by analogy to epithelial cells, can be either more columnar or more squamous in shape (Figure 2E). Importantly, the interphase cell long axis did not align well with the rachis surface and is therefore unlikely to contribute to spindle orientation relative to this surface in anaphase.

We next looked at the relationship between spindle orientation and the cell long axis during mitosis, as spindles can also respond to mitotic cell shape.^{16, 42, 43, 47, 48} We found that the orientation of the cell long axis just prior to anaphase onset was more likely to be parallel to the rachis surface than in interphase cells (Figures 2D and 2E). Accordingly, anaphase spindle orientation showed a moderate enrichment for angles aligned with the mitotic cell long axis (Figure 2F). However, spindles were most closely aligned with the mitotic cell long axis when this axis was perpendicular to the rachis normal and thus parallel to the rachis surface, while spindles were strongly aligned to the rachis surface irrespective of the orientation of the mitotic cell long axis (Figure 2G). Thus, during mitosis, the rachis surface, rather than mitotic cell shape, is the primary determinant of germ cell spindle orientation.

Dynein and LIN-5/NuMA are required for germ cell spindle orientation and germline tissue organization

Dynein and LIN-5/NuMA regulate spindle orientation in the *C. elegans* one-cell zygote,⁴⁹ but a role for these proteins in germ cells has not been assessed. We used the auxin-inducible degron (AID) system^{50, 51} to acutely deplete dynein heavy chain

(DHC-1) and LIN-5/NuMA specifically in the germ line. Treating L4 larvae with auxin for 40 min reduced germline DHC-1/dynein and LIN-5/NuMA to roughly 40% and 20% of their control levels, respectively (Figures 3A and 3B) and significantly decreased spindle movement during prometa/metaphase and spindle elongation in anaphase (Figures S3A and S2B), consistent with a substantial loss of cortical pulling forces. For technical reasons, we used the gonad surface as a proxy for the rachis surface and found that, under both conditions, the spindle orientation bias relative to the gonad surface was significantly reduced (Figure 3C). Spindle orientation relative to the gonadal D/P axis was also perturbed (Figure S3C). These results demonstrate that both dynein/DHC-1 and LIN-5/NuMA are required for proper spindle orientation in *C. elegans* germ cells.

In *C. elegans* embryos, as in other species,³ cortical loading of LIN-5/NuMA depends on two redundant G protein regulators, the LGN orthologs GPR-1 and GPR-2 (hereafter GPR-1/2).^{52, 53} We depleted GPR-1/2 by RNAi and found that, as in LIN-5/NuMA and DHC-1/dynein-depleted animals, germ cell spindle movements in prometa/metaphase and anaphase were reduced (Figures S3D and S3E), and a subset of germ cells were multipolar (Figure S3F), consistent with earlier reports suggesting a role for GPR-1/2 in chromosome segregation and spindle positioning.⁵³ Surprisingly, germ cell spindle orientation in these GPR-1/2-depleted animals was no different from control (Figure S3G). This suggests that, while GPR-1/2 are required for anaphase pulling forces in germ cells, they may not be required for proper spindle orientation (see [limitations of the study](#) section below).

We next asked whether depleting DHC-1/dynein or LIN-5/NuMA affected germline tissue organization by subjecting animals to auxin treatment for 6 h, during which most mitotically competent cells will have divided once.^{27, 54} We found that a 6-h depletion of either protein resulted in a notable alteration of rachis shape and increased variation in germ cell size (Figure 3D and S3H–K). In LIN-5/NuMA-depleted animals, rachis volume was reduced and the rachis tended to constrict and/or fragment, as seen by rachis discontinuity and an increase in the number of objects detected when we performed rachis surface renderings (Figures 3D–3F). In addition, germ cell volume was larger, on average, and more variable (Figure S3L), although this may be a consequence of defects in cell division.

Together, these results indicate that LIN-5/NuMA and DHC-1/dynein control germ cell spindle orientation and are required for maintenance of proper germline architecture during development.

The cortical distribution of LIN-5/NuMA predicts germ cell spindle orientation

Since LIN-5/NuMA is required for proper spindle orientation in germ cells, and its cortical localization correlates with sites of force generation in other cell types,^{3, 55} we examined its cortical localization in germ cells. We measured the fluorescence intensity of FP-tagged LIN-5/NuMA at the rachis, basal, and lateral cell cortices, in both interphase and mitotic germ cells, using a custom 3D line-scan method and normalizing the intensity of FP-tagged LIN-5/NuMA to the membrane signal at each cell cortex (Figures 4A–4C and S4A–S4C).

In interphase cells, LIN-5/NuMA was enriched on lateral and basal cortices, while its levels were low at the rachis surface

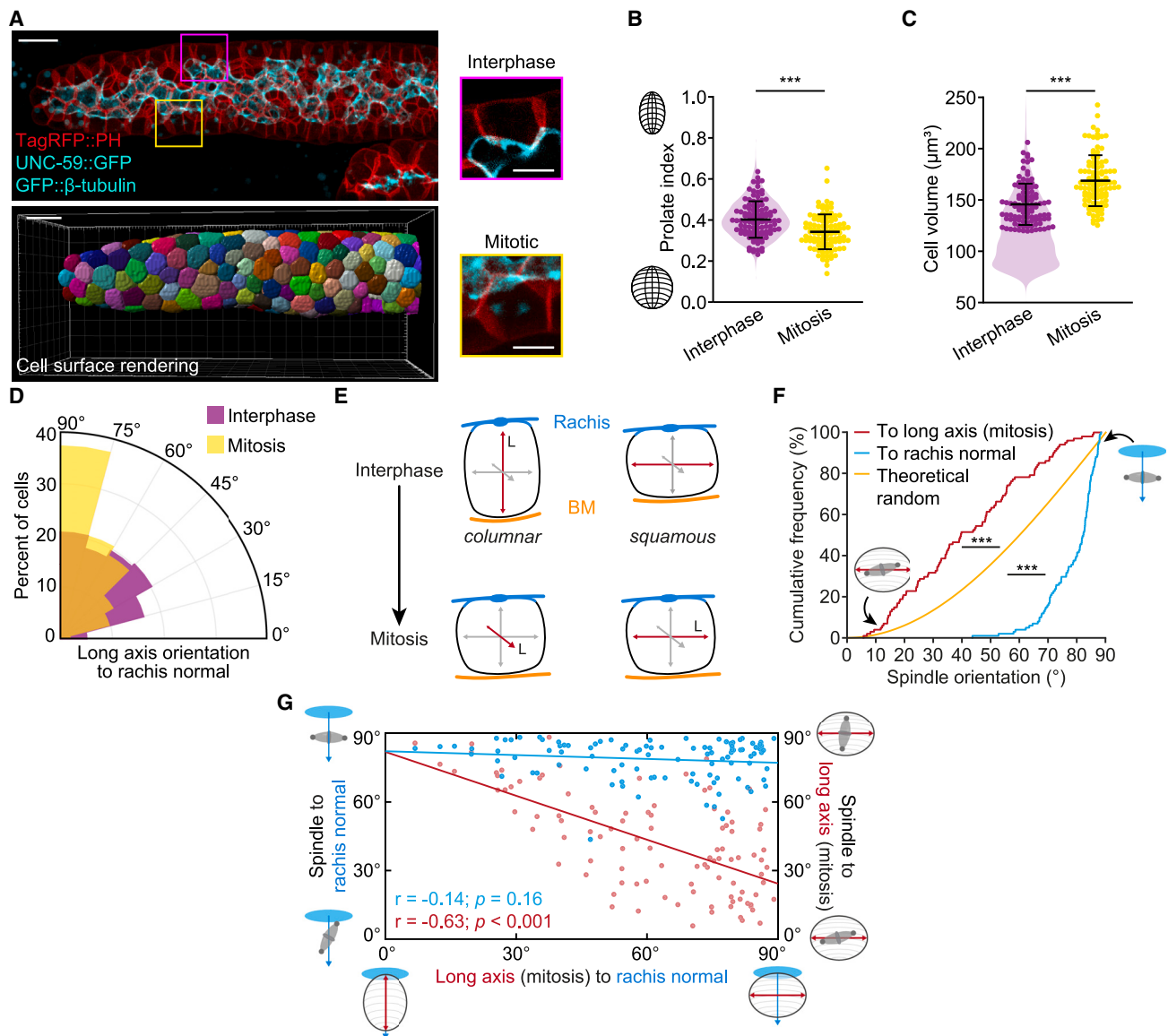


Figure 2. Spindle orientation to the rachis surface occurs independently of cell shape

(A) Maximum-intensity projection (top) and 3D cell surface rendering (bottom) of a distal gonad arm from an L4 larva expressing endogenously tagged UNC-59::GFP to mark the rachis (cyan), and GFP::β-tubulin and TagRFP::PH in the germ line, to mark spindles (cyan) and cell membranes (red), respectively. Scale bar, 10 μm. An interphase (magenta box) and a mitotic (yellow box) germ cell are shown to the right. Scale bar, 5 μm

(B and C) The prolate index (B) and cell volume (C) of germ cells in interphase and mitosis. For interphase cells, violin plots show the data for all cells and dots show the data used for comparison with mitotic cells. Interphase cells were selected based on cell volume by drawing a random set of cells from all interphase cells with a cell volume within ±2 standard deviations of the mean volume for mitotic cells. Each dot represents one cell. Bars represent the mean ± standard deviation.

(D) Rosette plot showing the orientation of the cell long axis in interphase (magenta) and mitosis (yellow) to the rachis normal.

(E) Schematic representation of interphase and mitotic germ cell shape, based on the measurements in (D), depicting configurations of the cell long axis relative to the rachis surface.

(F) Cumulative distribution of spindle angles in anaphase to the mitotic cell long axis (just prior to anaphase onset) and to the rachis normal for the same set of cells.

(G) Scatterplot showing the relationship between spindle orientation to the rachis normal (blue) and spindle orientation to the mitotic cell long axis (red) versus the orientation of the mitotic cell long axis to the rachis normal, with the Pearson's linear correlation coefficient (r) and p value shown below. Spindle orientation to the mitotic cell long axis depends on the orientation between the mitotic cell long axis and the rachis normal.

For all panels, *** $p < 0.001$. Summary statistics and statistical tests used are given in Table S3.

(Figure 4D). We observed a similar pattern in animals overexpressing a GFP-tagged version of GPR-1 in the germ line (Figure S4D). In mitotic cells, LIN-5/NuMA underwent a pronounced

change in its cortical association: while levels at the rachis surface remained low, the amount of LIN-5/NuMA on other cell cortices, particularly the basal cortex, was noticeably reduced

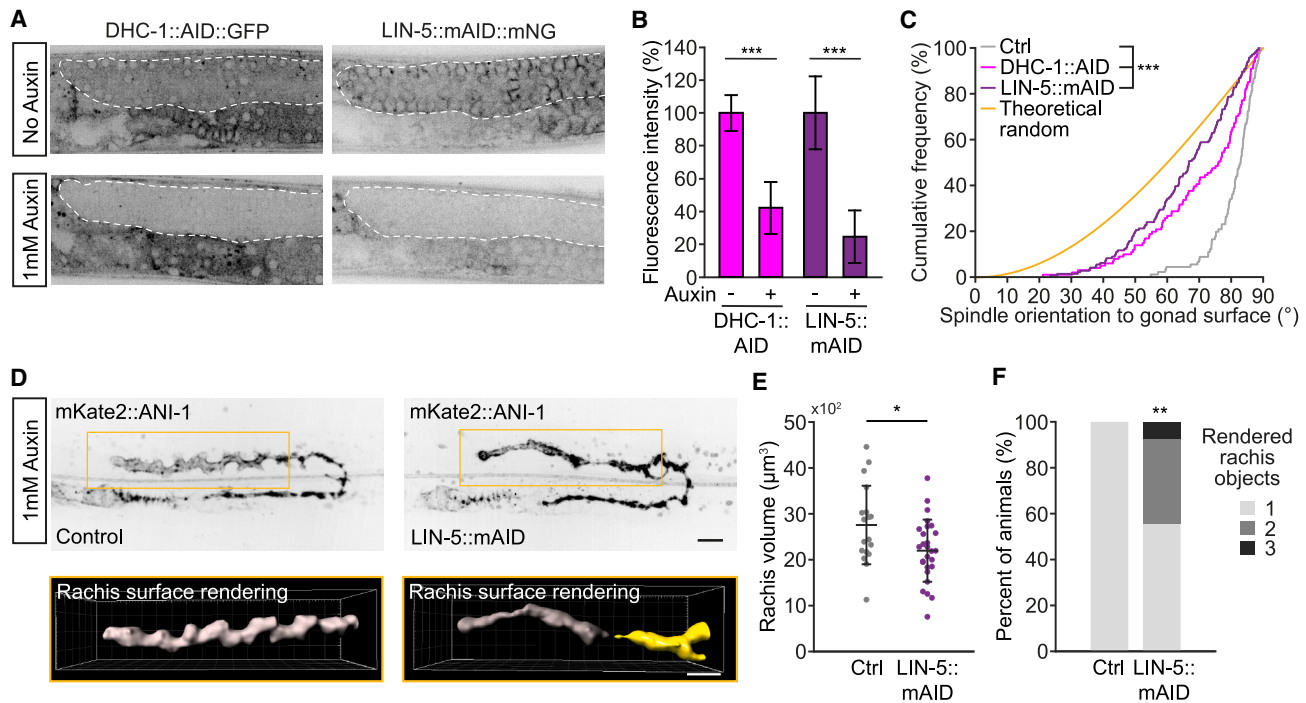


Figure 3. Dynein and LIN-5/NuMA are required for germ cell spindle orientation and germline tissue organization

(A) Confocal sections through the mid-plane of gonad arms from L4 larvae expressing DHC-1::AID::GFP (dynein, left) or LIN-5::mAID::mNG (NuMA, right), with a germline-specific TIR1 (*sun-1p::TIR1*), after a 40-min auxin treatment, as compared to untreated animals. The germ line is outlined in white. Scale bar, 10 μ m

(B) Quantification of the fluorescence intensity of each FP-tagged protein in the germ line. Measurements were normalized to the mean value for non-depleted germ lines.

(C) Cumulative distribution of spindle angles at anaphase to the gonad surface normal vector, comparing control animals to those depleted of DHC-1/dynein or LIN-5/NuMA as in (A) and (B). Depletion of either DHC-1/dynein or LIN-5/NuMA reduces the spindle orientation bias to the gonad surface. The theoretical random distribution (yellow) is shown for reference.

(D) Top: maximum-intensity projections of gonad arms from L4 larvae expressing mKate2::ANI-1, depleted (right) or not (left) of LIN-5/NuMA in the germ line by a 6-h auxin treatment. Bottom: reconstruction of the distal rachis surface using the mKate2::ANI-1 signal showing one rendered object in the non-depleted germ line (gray) and two objects in the depleted germ line (gray and yellow). Scale bars, 10 μ m

(E) Distal rachis volume in control and LIN-5/NuMA-depleted animals. Each dot represents the rachis for one gonad arm. Bars represent the mean \pm standard deviation.

(F) The number of rendered rachis objects in control and LIN-5/NuMA-depleted animals.

For all panels, * $p < 0.05$, ** $p < 0.01$, and *** $p < 0.001$. Summary statistics and statistical tests used are given in Table S3. See also Figure S3.

(Figure 4E). Timelapse images showed a loss of LIN-5/NuMA from the basal surface during prophase that was concomitant with the appearance of basally located LIN-5/NuMA puncta, likely at the nascent centrosomes (Figure 4F; Video S2). During prometa/metaphase, LIN-5/NuMA localization was highly dynamic, appearing as puncta on the lateral cortices that tracked with centrosome movements (Figure 4G; Video S3). Correspondingly, just prior to the start of pole separation at anaphase onset, we found that LIN-5/NuMA was enriched on lateral cortices along the spindle vector, and thus adjacent to centrosomes, relative to lateral cortices along the orthogonal vector (Figure 4E). In late anaphase/telophase, LIN-5/NuMA reappeared at the basal surface, seemingly in conjunction with the basal movement of the disassembling centrosomes (Figure 4H; Video S4).

Thus, during mitosis, cortical LIN-5/NuMA is dynamic, and its enrichment on lateral cell cortices along the spindle axis is consistent with its role in controlling the final orientation of cell di-

vision. Importantly, LIN-5/NuMA levels are consistently low at the germ cell's rachis surface, suggesting a relative lack of pulling forces on astral microtubules from this cortex, both as spindle orientation is established in prophase and maintained during mitosis.

Centrosome positioning during interphase and movement during prophase establish germ cell spindle orientation

The redistribution of LIN-5/NuMA from centrosomes to the basal cortex during mitotic exit raised the possibility that centrosomes might be positioned basally during interphase. To test this, we used animals bearing FP-tagged γ -tubulin and histone H2B to assess centrosome position relative to germ cell nuclei throughout the cell cycle. Visually, centrosomes were located close to the nucleus and toward the exterior of the gonad and thus the basal cell cortex (Figure 5A). We measured centrosome position on the nucleus relative to the rachis-basal axis for a

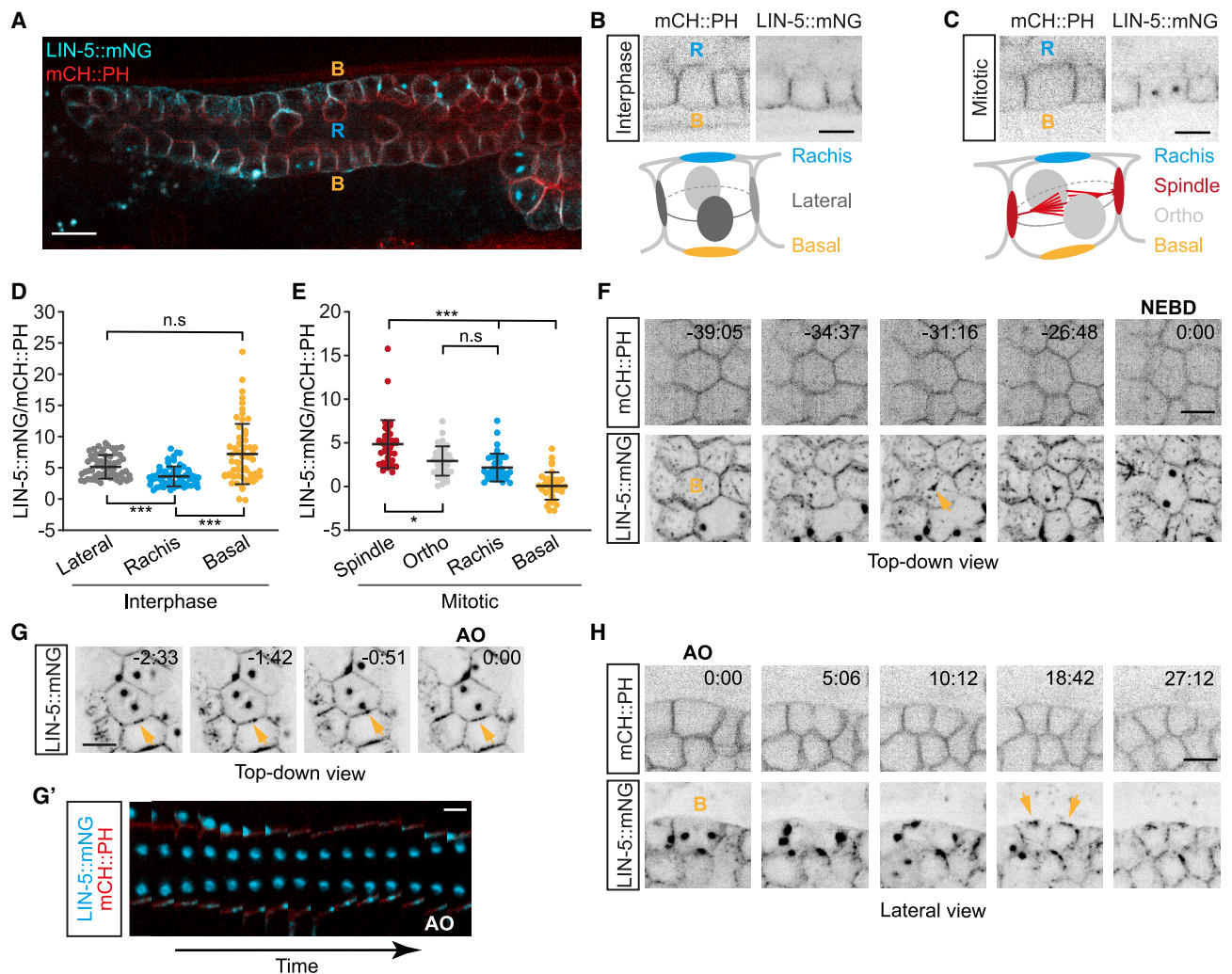


Figure 4. The cortical distribution of LIN-5/NuMA predicts germ cell spindle orientation

(A) Maximum-intensity projection of confocal sections through the middle of a gonad arm from an L4 larva expressing endogenously tagged LIN-5::mNG (NuMA, cyan) and germline-expressed mCH::PH to mark cell membranes (red). B, basal; R, rachis. Scale bar, 10 μ m
(B and C) Maximum-intensity projections (top) of germ cells during interphase (B) and mitosis (C) showing cell membranes (mCH::PH; left) and LIN-5::mNG (right) in inverted grayscale. Scale bars, 5 μ m. Schematic representations (bottom) depict the line-scan method used for fluorescence-intensity measurements at cell cortices along the rachis-basal and spindle/orthogonal or lateral axes.
(D and E) LIN-5::mNG cortical fluorescence intensity, normalized to the membrane mCH::PH signal, in interphase (D) and mitotic (anaphase onset; E) germ cells, as depicted in (B) and (C). Each dot represents one cell. Bars represent the mean \pm standard deviation. n.s. $p > 0.05$; * $p < 0.05$; *** $p < 0.001$.
(F) Maximum-intensity projections of the mCH::PH (top) and LIN-5::mNG (bottom) signal at the basal surface (top-down view) of a germ cell progressing through prophase. Time is shown in minutes relative to nuclear envelop breakdown (NEBD). B, basal (marks the cell of interest). Arrowhead indicates LIN-5::mNG puncta at the basal surface. Scale bar, 5 μ m.
(G) Maximum-intensity projections of the LIN-5::mNG signal at the mid-plane of a germ cell in mitosis (top-down view). Time is shown in minutes relative to anaphase onset (AO). Arrowheads indicate LIN-5::mNG at the lateral cortex adjacent to the spindle pole. Scale bar, 5 μ m. (G') Kymograph along the spindle vector for the cell shown in (G) with mCH::PH (red) and LIN-5::mNG (cyan) showing the formation and dissolution of a LIN-5::mNG focus (lower membrane; bright spot adjacent to upper membrane is the spindle pole from a neighboring cell). Timescale bar, 17 s
(H) Maximum-intensity projections of the mCH::PH (top) and LIN-5::mNG (bottom) signal at the mid-plane of a germ cell in anaphase showing a lateral view of the basal surface, B, and the basal localization of LIN-5::mNG (arrowheads) upon mitotic exit. Time is shown in minutes relative to AO. Scale bar, 5 μ m.
Summary statistics and statistical tests used are given in Table S3. See also Figure S4 and Videos S2, S3, and S4.

population of interphase germ cells (here defined as cells with a single γ -tubulin-positive focus) and found that centrosomes were largely located along the basal 70% of the nuclear surface (Figure 5B). Thus, during interphase, centrosomes are posi-

tioned on the basal face of the nucleus, roughly opposite to the rachis surface. This is distinct from the lateral position centrosomes occupy during anaphase, suggesting that they are repositioned upon mitotic exit.

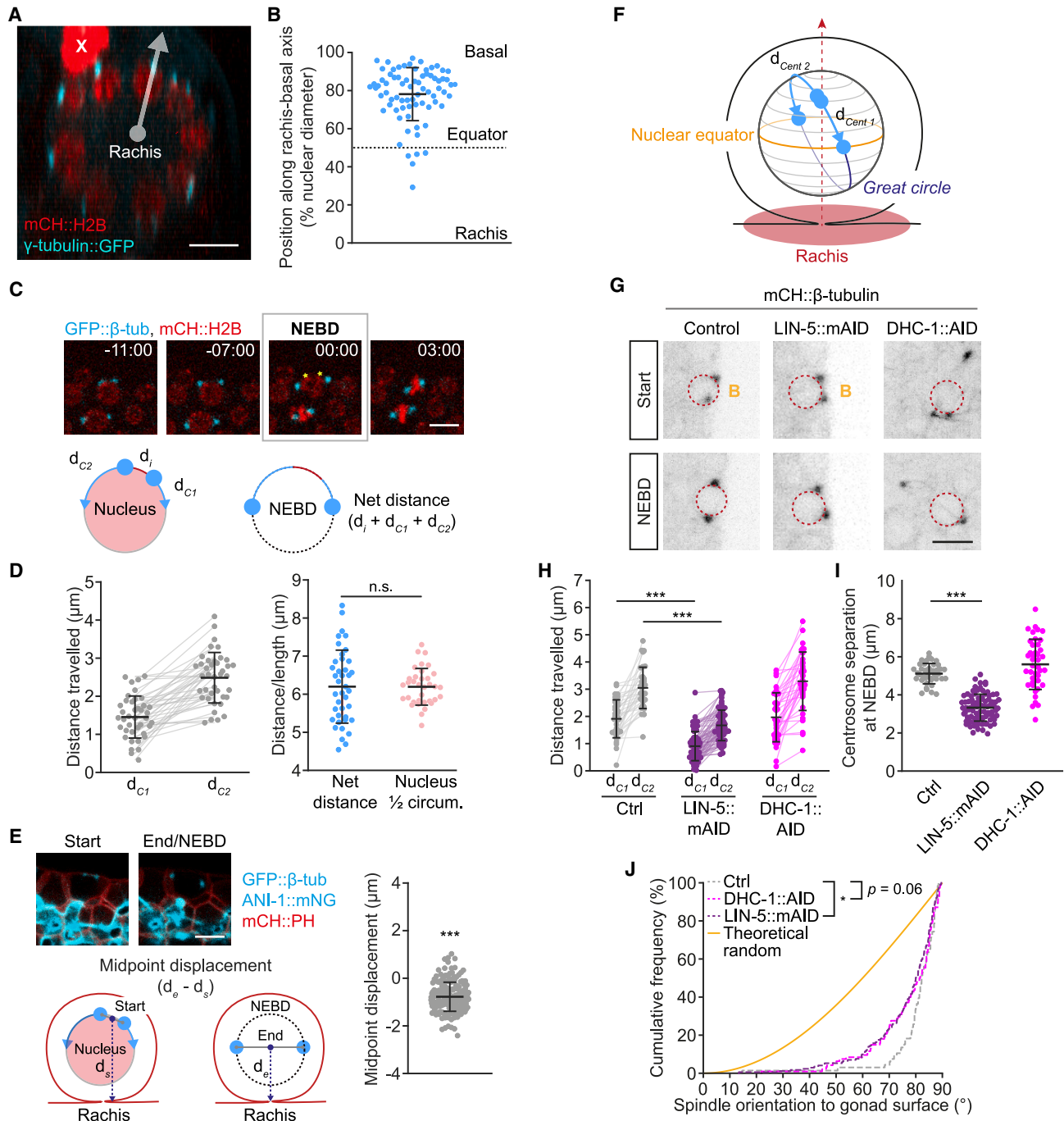


Figure 5. Centrosome positioning during interphase and movement during prophase establish germ cell spindle orientation

(A) Maximum-intensity projection of a cross-sectional view of a distal gonad arm from an L4 larva expressing mCH::HIS-58(H2B) to mark nuclei (red) and TBG-1(γ -tubulin)::GFP to mark centrosomes (cyan). The gray line depicts the rachis-basal axis for the nucleus at the top right. The bright red blob (X) is a somatic nucleus outside of the gonad.

(B) The position of centrosomes in interphase relative to the rachis-basal axis for each cell expressed as a percentage of nuclear diameter, with 100% and 0% indicating the basal and rachis poles, respectively.

(C) Top: maximum-intensity projections of germ cells expressing mCH::HIS-11(H2B) (red) and GFP:: β -tubulin (cyan). Time is shown in minutes relative to nuclear envelop breakdown (NEBD). Yellow asterisks represent centrosome position at the start of tracking. Bottom: schematic depicting centrosome migration (blue) around the nuclear surface (pink) during prophase. Net distance traveled equals the sum of centrosome-to-centrosome distance at the start of tracking (d_i) plus the distance traveled by each centrosome around the nucleus prior to NEBD (d_{C1} and d_{C2}).

(legend continued on next page)

The basal position of centrosomes during interphase raised the question of how spindles assemble parallel to the rachis surface in the following mitosis. To assess this, we tracked centrosomes throughout prophase and found that both centrosomes migrated, with one centrosome typically traveling further than its partner (Figures 5C and 5D). After accounting for centrosome separation prior to the start of tracking (see Figure 5C), the combined distance traveled by pairs of centrosomes was roughly equivalent to half the nuclear circumference (Figure 5D). To determine whether this movement was directed toward the rachis surface, we measured the displacement of the midpoint between centrosomes along the rachis-basal axis and found that it moved closer to the cell's rachis surface (Figure 5E). Together, these results suggest that both centrosomes traverse the shortest possible route from a basal starting point, to reach opposite sides of the nucleus at the nuclear equator, effectively traveling along a nuclear "great circle." This pattern of migration ensures that the spindle forms parallel to the rachis surface at NEBD (Figure 5F).

The directed movement of centrosomes requires a directional bias in the forces driving their migration.⁵⁶ Given the polarized cortical distribution of LIN-5/NuMA (Figure 4), we asked whether it was required for these forces. We found that most germ cells undergoing prophase after 40 min of AID-mediated LIN-5/NuMA depletion showed reduced centrosome movement during prophase and incomplete centrosome separation at NEBD (Figures 5G–5I). The difference in distance traveled between centrosome pairs was also slightly reduced, although this result was not statistically significant. By contrast, in DHC-1/dynein-depleted cells, net centrosome movement during prophase was similar to control, but centrosome separation at NEBD was more variable (Figures 5H and 5I; $p < 0.001$, Bartlett test for equal variance), with some centrosomes detaching from the nucleus altogether (Figures 5G and S5A). These results suggest that LIN-5/NuMA plays a major role in generating the forces driving centrosome separation, while the dominant role for dynein is to anchor centrosomes to the nuclear surface, where DHC-1 is most prominently localized (Figure S5B; see Zhou et al.⁵⁷). Accordingly, in both depleted conditions, spindle orientation at NEBD tended to be less strictly aligned with the rachis surface than in control cells (Figure 5J).

Together, our data support the notion that exclusion of LIN-5/NuMA from the germ cell's rachis surface, combined with its

removal from the cell's basal cortex in early mitosis, biases centrosome movement during prophase to establish spindle orientation parallel to the rachis surface at NEBD.

DISCUSSION

Here, we demonstrate that *C. elegans* germ cells divide parallel to the rachis surface and thus within the plane of the germline tissue during gonad development. These oriented cell divisions are driven by a strong bias in mitotic spindle orientation perpendicular to the cell rachis-basal axis, which relies on the activity of the microtubule motor protein dynein and its regulator LIN-5/NuMA. Our results support a model (Figure 6) in which the polarized localization of LIN-5/NuMA throughout the cell cycle establishes germ cell spindle orientation during prophase and maintains it through anaphase. Here, the loss of LIN-5/NuMA from the basal cortex during prophase favors the migration of centrosomes around the nucleus, from their starting basal position toward the cell equator, while the lack of LIN-5/NuMA at the rachis surface ensures that they adopt an orientation parallel to the surface of the rachis at NEBD. The maintenance of LIN-5/NuMA on lateral cortices along the spindle axis after NEBD serves to both stabilize spindle orientation and promote spindle elongation in anaphase. As cells exit mitosis, LIN-5/NuMA returns to the basal cortex, along with the disassembling centrosomes, preparing cells for the following division. This process, reiterated at each round of cell division, provides a mechanism to couple germ cell division to planar tissue organization throughout development.

This model supposes a key role for centrosome positioning in interphase and centrosome dynamics in prophase in establishing proper spindle orientation. Equal centrosome movement in prophase, from the site of centriole duplication toward opposite sides of the nucleus by NEBD, sets spindles up perpendicular to the preceding axis of cell division.⁵⁸ Several mechanisms have been described by which cells overcome this geometric constraint, including tethering one centrosome while the other performs the entirety of migration around the nucleus,^{59–61} and directed rotation of centrosome pairs, with the nucleus they flank, after centrosome separation.⁶² *C. elegans* germ cells have a seemingly different solution to this problem: by positioning the centrosome inherited from the preceding cell division

(D) Left: distanced traveled by centrosomes, as depicted in (C), with lines connecting centrosomes from the same cell. Right: net distance traveled by centrosome pairs, as depicted in (C), compared to the nucleus half circumference.

(E) Top: maximum-intensity projections (top) of a mitotic germ cell at the start of centrosome tracking in prophase and at NEBD with mNG::ANI-1 (cyan), GFP:: β -tubulin (cyan) and TagRFP::PH (red) marking the rachis, spindle poles, and cell membranes, respectively. Schematic representations (bottom left) and measurements (right) of centrosome-to-centrosome midpoint displacement relative to the rachis surface from the start of centrosome tracking (d_{c}) to the end (d_{e}) of prophase (NEBD). Values <0 occur when the midpoint is closer to the rachis surface at NEBD.

(F) Schematic representation of centrosome migration during prophase as inferred from the measurements in (A)–(E).

(G) Maximum-intensity projections of mCH:: β -tubulin in germ cells at the start of centrosome tracking (top) and at NEBD (bottom) in control animals (left) and animals depleted of LIN-5/NuMA (middle) or DHC-1/dynein (right) by a 40-min auxin treatment. The nucleus is outlined in red. B, basal. The DHC-1/dynein-depleted cell is at the top surface of the gonad and its basal surface is not visible in the projection.

(H and I) The distanced traveled around the nucleus in prophase for pairs of centrosomes (H) and centrosome-to-centrosome distance (separation) at NEBD (I) in control versus LIN-5/NuMA- or DHC-1/dynein-depleted cells.

(J) Cumulative distribution of spindle angles at NEBD to the gonad surface normal vector, comparing control animals to those depleted of DHC-1/dynein or LIN-5/NuMA. The theoretical random distribution (yellow) is shown for reference.

In all panels, dots represent individual centrosomes (D left and H) or per-cell values (B and D right, E right, and I), and bars represent the mean \pm standard deviation. n.s., $p > 0.05$; * $p < 0.05$; *** $p < 0.001$. Scale bars, 5 μm . Summary statistics and statistical tests used are given in Table S3. See also Figure S5.

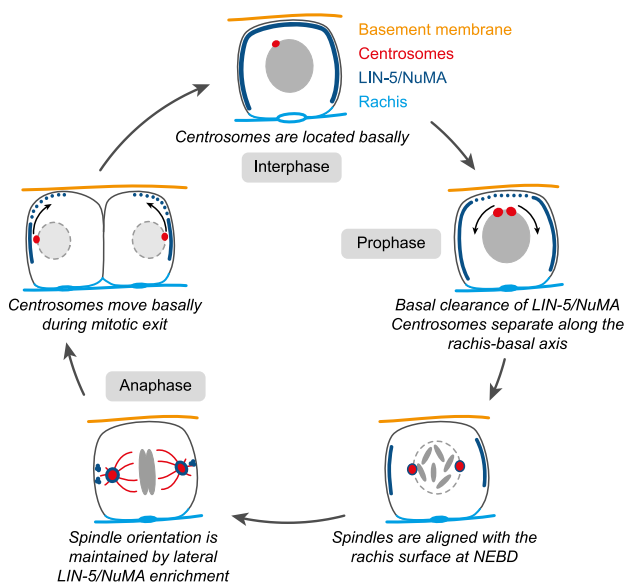


Figure 6. Model for centrosome positioning and spindle orientation during the *C. elegans* germ cell cycle

See main text for details.

basally, equal centrosome migration during prophase favors spindle orientation parallel to the rachis surface across subsequent rounds of cell division.

The basal location of germ cell centrosomes during interphase raises the question of how they acquire this position. One possibility is that cortical rearrangements during mitotic exit drag disassembling centrosomes basally. Another, non-exclusive scenario is that the redistribution of LIN-5/NuMA to the basal cortex favors centrosome pulling toward this site. High-resolution timelapse imaging to correlate centrosome dynamics with cortical movements and LIN-5/NuMA cortical enrichments during mitotic exit are needed to further address this idea.

We note that interphase centrosomes are not perfectly aligned with the basal pole of the nucleus, nor is centrosome migration during prophase perfectly symmetric. We infer that ensuring proper spindle orientation at NEBD requires asymmetries in the forces driving prophase centrosome migration, or that these asymmetries are eventually corrected after NEBD, when spindles undergo rotational movements. In addition, we find that simply setting spindles up parallel to the rachis surface at NEBD is unlikely to ensure a strong orientation bias through anaphase, implying that an active mechanism maintains spindle orientation throughout mitosis. Our results suggest that the forces dictating prophase centrosome migration and the final orientation of the spindle in anaphase hinge on the spatiotemporal regulation of LIN-5/NuMA.

How might this regulation be achieved? Our work suggests that LIN-5/NuMA's cortical association in germ cells is cell cycle dependent. LIN-5/NuMA can be phosphorylated by mitotic kinases, including Cdk1,^{63–65} Plk1,⁶⁶ and Aurora A,^{67,68} any of which could impact its cortical loading in *C. elegans* germ cells. LIN-5/NuMA's exclusion from the rachis surface throughout the cell cycle suggests that its cortical distribution is also influenced

by germ cell rachis-basal polarity. *C. elegans* germline architecture is defined by the presence of actomyosin-rich intercellular bridges connecting germ cells to the rachis.^{29,33} However, the presence of this bridge is unlikely to account for LIN-5/NuMA polarization, as rachis bridges are effectively closed during mitosis, yet association between LIN-5/NuMA and the rachis surface does not change (Figures 4D and 4E), and LIN-5/NuMA is excluded from the entire rachis surface, including regions away from the rachis bridge (Figures 4A–4C). Instead, as anisotropies in actomyosin-driven tension influence the activity of force generators and spindle orientation in other contexts,⁶⁹ the enrichment of actomyosin and/or the mechanical properties of the rachis cortex may locally restrict the amount of LIN-5/NuMA, perhaps by excluding GPR-1/2 (Figure S4D).

Finally, during mitosis, LIN-5/NuMA is enriched on lateral germ cell cortices, but only those behind the spindle poles, where it appears as transient foci. This resembles what has been seen in several other cell types, where clustering of the force-generating machinery contributes to spindle orientation.^{3,70,71} In addition, evidence from several systems suggests that astral microtubules can direct the cortical deposition of force-generating complexes to focus pulling forces at sites of microtubule-membrane contact.^{72–76} It is therefore possible that exclusion of LIN-5/NuMA from the rachis surface is sufficient to maintain spindles parallel to this surface, while spindle-driven focusing of the force-generating machinery gives spindles flexibility within the plane of the tissue to respond to other cues, including the gonadal D/P axis. Future work is necessary to determine the nature of these cues and the precise mechanism by which force generation is consolidated on germ cell lateral membranes.

In summary, our work suggests that *C. elegans* germ cells undergo oriented cell divisions by controlling the distribution of cortical force generators in both time and space to ensure that the mitotic spindle is established and maintained within the tissue plane. This work presents an alternative model by which spindle orientation and oriented cell division can be achieved and highlights the mechanistic plasticity of these processes during animal development.

Limitations of the study

We found that long-term depletion of LIN-5/NuMA resulted in germline tissue disorganization, with a notable impact on rachis morphology. This contrasts with what has been found in some epithelial tissues, where defects in spindle orientation do not cause major disruptions in epithelial tissue organization.^{77,78} The distinctive syncytial organization of the *C. elegans* germ line may increase reliance on spindle orientation and/or preclude the compensatory mechanisms (reinsertion⁷⁷ and apoptosis⁷⁸) that deal with mispositioned cells in epithelia. However, in our current study, long-term LIN-5/NuMA depletion led to an increase in germ cell size, suggesting that cell division is also perturbed. Thus, we cannot differentiate between defects in rachis organization resulting from mis-oriented cell divisions versus those that may be an indirect consequence of failed cell divisions. Additional experiments are needed to establish a direct link between spindle orientation and tissue organization in the *C. elegans* germ line. Furthermore, we found that depletion of GPR-1/2 led to defects in germ cell spindle dynamics but did

not perturb spindle orientation. While these results suggest that the dynein-mediated pulling forces that orient spindles in germ cells are independent of GPR-1/2, we cannot exclude the possibility that RNAi is not sufficient to reduce GPR-1/2 activity below the threshold required for proper spindle orientation. Tools to acutely perturb these regulators, such as AID-mediated depletion, will be needed to better establish the role of GPR-1/2.

RESOURCE AVAILABILITY

Lead contact

Further information and requests for resources and reagents should be directed to and will be fulfilled by the lead contact, Abigail Gerhold (abigail.gerhold@mcgill.ca).

Materials availability

C. elegans strains used in this study are available upon request from the lead contact.

Data and code availability

- Microscopy data reported in this study are available upon request from the [lead contact](#).
- All original code is publicly available and has been deposited at <https://github.com/VincentPoupart/Zellag2024> and <https://github.com/yifnzhao/CentTracker>.
- Any additional information required to reanalyze the data reported in this paper is available from the [lead contact](#) upon request.

ACKNOWLEDGMENTS

We thank Arshad Desai, Amy Maddox, Pablo Lara-Gonzalez, and Benjamin Lacroix for sharing strains and Christian Charboneau of IRIC's Bio-imaging facility for technical assistance. Some strains were provided by the *Caenorhabditis* Genetics Center, which is funded by the NIH Office of Research Infrastructure Programs (P40 OD010440). The mNG-mom-5 plasmid was provided by Jennifer Heppert and Bob Goldstein. R.M.Z. holds scholarships from the Natural Sciences and Engineering Research Council of Canada (NSERC) and the Fonds de recherche du Québec – Nature et Technologies (FRQ-NT). This work was funded by grants from JSPS KAKENHI (23K05836) to T.N. and the Canadian Institutes of Health Research (PJT-153283) to J.-C.L. and A.R.G.

AUTHOR CONTRIBUTIONS

Conceptualization, R.M.Z., V.P., J.-C.L., and A.R.G.; methodology, R.M.Z., V.P., J.-C.L., and A.R.G.; software, R.M.Z., V.P., and A.R.G.; formal analysis, R.M.Z., V.P., T.N., and A.R.G.; investigation, R.M.Z., V.P., and T.N.; data curation, R.M.Z. and V.P.; writing – original draft, R.M.Z., J.-C.L., and A.R.G.; writing – review & editing, R.M.Z., V.P., T.N., J.-C.L., and A.R.G.; visualization, R.M.Z., V.P., and A.R.G.; funding acquisition, J.-C.L. and A.R.G.

DECLARATION OF INTERESTS

The authors declare no competing interests.

STAR★METHODS

Detailed methods are provided in the online version of this paper and include the following:

- [KEY RESOURCES TABLE](#)
- [EXPERIMENTAL MODEL AND STUDY PARTICIPANT DETAILS](#)
 - *C. elegans* strain maintenance
- [METHOD DETAILS](#)
 - Generation of mAID:mNG-tagged LIN-5
 - Worm mounting and live imaging

- Auxin treatment
- RNAi treatment
- Gonad explants
- Germ cell centrosome tracking and scoring of mitotic events
- Cell surface rendering and cell long axis extraction
- Defining the gonadal D/P axis
- Rachis and gonad surface rendering
- Determining the orientation of the rachis or gonad surface for each cell
- Measuring spindle and cell long axis orientations
- Cortical fluorescence intensity measurements
- Analysis of centrosome movement and position in prophase
- Measuring centrosome position in interphase cells
- [QUANTIFICATION AND STATISTICAL ANALYSIS](#)

SUPPLEMENTAL INFORMATION

Supplemental information can be found online at <https://doi.org/10.1016/j.celrep.2025.115296>.

Received: September 6, 2024

Revised: December 6, 2024

Accepted: January 20, 2025

Published: February 12, 2025

REFERENCES

1. Morin, X., and Bellaïche, Y. (2011). Mitotic spindle orientation in asymmetric and symmetric cell divisions during animal development. *Dev. Cell* 21, 102–119. <https://doi.org/10.1016/j.devcel.2011.06.012>.
2. Lechler, T., and Mapelli, M. (2021). Spindle positioning and its impact on vertebrate tissue architecture and cell fate. *Nat. Rev. Mol. Cell Biol.* 22, 691–708. <https://doi.org/10.1038/s41580-021-00384-4>.
3. Kiyomitsu, T. (2019). The cortical force-generating machinery: how cortical spindle-pulling forces are generated. *Curr. Opin. Cell Biol.* 60, 1–8. <https://doi.org/10.1016/j.cob.2019.03.001>.
4. Zheng, Z., Zhu, H., Wan, Q., Liu, J., Xiao, Z., Siderovski, D.P., and Du, Q. (2010). LGN regulates mitotic spindle orientation during epithelial morphogenesis. *J. Cell Biol.* 189, 275–288. <https://doi.org/10.1083/jcb.200910021>.
5. Peyre, E., Jaouen, F., Saadaoui, M., Haren, L., Merdes, A., Durbec, P., and Morin, X. (2011). A lateral belt of cortical LGN and NuMA guides mitotic spindle movements and planar division in neuroepithelial cells. *J. Cell Biol.* 193, 141–154. <https://doi.org/10.1083/jcb.201101039>.
6. Gloerich, M., Bianchini, J.M., Siemers, K.A., Cohen, D.J., and Nelson, W.J. (2017). Cell division orientation is coupled to cell-cell adhesion by the E-cadherin/LGN complex. *Nat. Commun.* 8, 13996. <https://doi.org/10.1038/ncomms13996>.
7. Guilgur, L.G., Prudêncio, P., Ferreira, T., Pimenta-Marques, A.R., and Martinho, R.G. (2012). *Drosophila* aPKC is required for mitotic spindle orientation during symmetric division of epithelial cells. *Development* 139, 503–513. <https://doi.org/10.1242/dev.071027>.
8. Hao, Y., Du, Q., Chen, X., Zheng, Z., Balsbaugh, J.L., Maitra, S., Shabanowitz, J., Hunt, D.F., and Macara, I.G. (2010). Par3 controls epithelial spindle orientation by aPKC-mediated phosphorylation of apical Pins. *Curr. Biol.* 20, 1809–1818. <https://doi.org/10.1016/j.cub.2010.09.032>.
9. Nakajima, Y.-i., Meyer, E.J., Kroesen, A., McKinney, S.A., and Gibson, M.C. (2013). Epithelial junctions maintain tissue architecture by directing planar spindle orientation. *Nature* 500, 359–362. <https://doi.org/10.1038/nature12335>.
10. Saadaoui, M., Machicoane, M., di Pietro, F., Etoc, F., Echard, A., and Morin, X. (2014). Dlg1 controls planar spindle orientation in the neuroepithelium through direct interaction with LGN. *J. Cell Biol.* 206, 707–717. <https://doi.org/10.1083/jcb.201405060>.

11. Carminati, M., Gallini, S., Pirovano, L., Alfieri, A., Bisi, S., and Mapelli, M. (2016). Concomitant binding of Afadin to LGN and F-actin directs planar spindle orientation. *Nat. Struct. Mol. Biol.* 23, 155–163. <https://doi.org/10.1038/nsmb.3152>.
12. Fernandez-Minan, A., Martin-Bermudo, M.D., and Gonzalez-Reyes, A. (2007). Integrin signaling regulates spindle orientation in *Drosophila* to preserve the follicular-epithelium monolayer. *Curr. Biol.* 17, 683–688. <https://doi.org/10.1016/j.cub.2007.02.052>.
13. Finegan, T.M., Na, D., Cammarota, C., Skeeters, A.V., Nádasi, T.J., Dawney, N.S., Fletcher, A.G., Oakes, P.W., and Bergstralh, D.T. (2019). Tissue tension and not interphase cell shape determines cell division orientation in the *Drosophila* follicular epithelium. *EMBO J.* 38, e100072. <https://doi.org/10.15252/embj.2018100072>.
14. Hart, K.C., Tan, J., Siemers, K.A., Sim, J.Y., Pruitt, B.L., Nelson, W.J., and Glierich, M. (2017). E-cadherin and LGN align epithelial cell divisions with tissue tension independently of cell shape. *Proc. Natl. Acad. Sci. USA* 114, E5845–E5853. <https://doi.org/10.1073/pnas.1701703114>.
15. Scarpa, E., Finet, C., Blanchard, G.B., and Sanson, B. (2018). Actomyosin-Driven Tension at Compartmental Boundaries Orients Cell Division Independently of Cell Geometry In Vivo. *Dev. Cell* 47, 727–740.e6. <https://doi.org/10.1016/j.devcel.2018.10.029>.
16. Campinho, P., Behrndt, M., Ranft, J., Risler, T., Minc, N., and Heisenberg, C.P. (2013). Tension-oriented cell divisions limit anisotropic tissue tension in epithelial spreading during zebrafish epiboly. *Nat. Cell Biol.* 15, 1405–1414. <https://doi.org/10.1038/ncb2869>.
17. Wyatt, T.P.J., Harris, A.R., Lam, M., Cheng, Q., Bellis, J., Dimitracopoulos, A., Kabla, A.J., Charras, G.T., and Baum, B. (2015). Emergence of homeostatic epithelial packing and stress dissipation through divisions oriented along the long cell axis. *Proc. Natl. Acad. Sci. USA* 112, 5726–5731. <https://doi.org/10.1073/pnas.1420585112>.
18. Mao, Y., Tournier, A.L., Hoppe, A., Kester, L., Thompson, B.J., and Tapon, N. (2013). Differential proliferation rates generate patterns of mechanical tension that orient tissue growth. *EMBO J.* 32, 2790–2803. <https://doi.org/10.1038/emboj.2013.197>.
19. Gibson, W.T., Veldhuis, J.H., Rubinstein, B., Cartwright, H.N., Perrimon, N., Brodland, G.W., Nagpal, R., and Gibson, M.C. (2011). Control of the mitotic cleavage plane by local epithelial topology. *Cell* 144, 427–438. <https://doi.org/10.1016/j.cell.2010.12.035>.
20. Bosveld, F., Markova, O., Guirao, B., Martin, C., Wang, Z., Pierre, A., Balakireva, M., Gague, I., Ainslie, A., Christophorou, N., et al. (2016). Epithelial tricellular junctions act as interphase cell shape sensors to orient mitosis. *Nature* 530, 495–498. <https://doi.org/10.1038/nature16970>.
21. Nestor-Bergmann, A., Stooke-Vaughan, G.A., Goddard, G.K., Starborg, T., Jensen, O.E., and Woolner, S. (2019). Decoupling the Roles of Cell Shape and Mechanical Stress in Orienting and Cueing Epithelial Mitosis. *Cell Rep.* 26, 2088–2100.e4. <https://doi.org/10.1016/j.celrep.2019.01.102>.
22. Tang, Z., Hu, Y., Wang, Z., Jiang, K., Zhan, C., Marshall, W.F., and Tang, N. (2018). Mechanical Forces Program the Orientation of Cell Division during Airway Tube Morphogenesis. *Dev. Cell* 44, 313–325.e5. <https://doi.org/10.1016/j.devcel.2017.12.013>.
23. Gong, Y., Mo, C., and Fraser, S.E. (2004). Planar cell polarity signalling controls cell division orientation during zebrafish gastrulation. *Nature* 430, 689–693. <https://doi.org/10.1038/nature02796>.
24. Mao, Y., Tournier, A.L., Bates, P.A., Gale, J.E., Tapon, N., and Thompson, B.J. (2011). Planar polarization of the atypical myosin Dachs orients cell divisions in *Drosophila*. *Genes Dev.* 25, 131–136. <https://doi.org/10.1101/gad.610511>.
25. Baena-Lopez, L.A., Baonza, A., and Garcia-Bellido, A. (2005). The orientation of cell divisions determines the shape of *Drosophila* organs. *Curr. Biol.* 15, 1640–1644. <https://doi.org/10.1016/j.cub.2005.07.062>.
26. Negishi, T., Miyazaki, N., Murata, K., Yasuo, H., and Ueno, N. (2016). Physical association between a novel plasma-membrane structure and centrosome orients cell division. *Elife* 5, e16550. <https://doi.org/10.7554/eLife.16550>.
27. Hubbard, E.J.A., and Schedl, T. (2019). Biology of the *Caenorhabditis elegans* Germline Stem Cell System. *Genetics* 213, 1145–1188. <https://doi.org/10.1534/genetics.119.300238>.
28. Kimble, J., and Seidel, H.S. (2013). *C. elegans* germline stem cells and their niche (StemBook). <https://doi.org/10.3824/stembook.1.95.1>.
29. Hirsh, D., Oppenheim, D., and Klass, M. (1976). Development of the reproductive system of *Caenorhabditis elegans*. *Dev. Biol.* 49, 200–219. [https://doi.org/10.1016/0012-1606\(76\)90267-0](https://doi.org/10.1016/0012-1606(76)90267-0).
30. Hall, D.H., Winfrey, V.P., Blaeuer, G., Hoffman, L.H., Furuta, T., Rose, K.L., Hobert, O., and Greenstein, D. (1999). Ultrastructural features of the adult hermaphrodite gonad of *Caenorhabditis elegans*: relations between the germ line and soma. *Dev. Biol.* 212, 101–123. <https://doi.org/10.1006/dbio.1999.9356>.
31. Amini, R., Goupil, E., Labella, S., Zetka, M., Maddox, A.S., Labbé, J.C., and Chartier, N.T. (2014). *C. elegans* Anillin proteins regulate intercellular bridge stability and germline syncytial organization. *J. Cell Biol.* 206, 129–143. <https://doi.org/10.1083/jcb.201310117>.
32. Priti, A., Ong, H.T., Toyama, Y., Padmanabhan, A., Dasgupta, S., Krajnc, M., and Zaidel-Bar, R. (2018). Syncytial germline architecture is actively maintained by contraction of an internal actomyosin corset. *Nat. Commun.* 9, 4694. <https://doi.org/10.1038/s41467-018-07149-2>.
33. Gerhold, A.R., Labbé, J.C., and Singh, R. (2022). Uncoupling cell division and cytokinesis during germline development in metazoans. *Front. Cell Dev. Biol.* 10, 1001689. <https://doi.org/10.3389/fcell.2022.1001689>.
34. Seidel, H.S., Smith, T.A., Evans, J.K., Stamper, J.Q., Mast, T.G., and Kimble, J. (2018). *C. elegans* germ cells divide and differentiate in a folded tissue. *Dev. Biol.* 442, 173–187. <https://doi.org/10.1016/j.ydbio.2018.07.013>.
35. Bauer, J., Poupart, V., Goupil, E., Nguyen, K.C.Q., Hall, D.H., and Labbé, J.C. (2021). The initial expansion of the *C. elegans* syncytial germ line is coupled to incomplete primordial germ cell cytokinesis. *Development* 148, dev199633. <https://doi.org/10.1242/dev.199633>.
36. Agarwal, P., Shemesh, T., and Zaidel-Bar, R. (2022). Directed cell invasion and asymmetric adhesion drive tissue elongation and turning in *C. elegans* gonad morphogenesis. *Dev. Cell* 57, 2111–2126.e6. <https://doi.org/10.1016/j.devcel.2022.08.003>.
37. Zellag, R.M., Zhao, Y., Poupart, V., Singh, R., Labbé, J.C., and Gerhold, A.R. (2021). CentTracker: a trainable, machine-learning-based tool for large-scale analyses of *Caenorhabditis elegans* germline stem cell mitosis. *Mol. Biol. Cell* 32, 915–930. <https://doi.org/10.1091/mbc.E20-11-0716>.
38. Zellag, R.M., Zhao, Y., and Gerhold, A.R. (2022). Live-cell Imaging and Analysis of Germline Stem Cell Mitosis in *Caenorhabditis elegans*. *Bio. Protoc.* 12, e4272. <https://doi.org/10.21769/BioProtoc.4272>.
39. Rehain-Bell, K., Love, A., Werner, M.E., MacLeod, I., Yates, J.R., 3rd, and Maddox, A.S. (2017). A Sterile 20 Family Kinase and Its Co-factor CCM-3 Regulate Contractile Ring Proteins on Germline Intercellular Bridges. *Curr. Biol.* 27, 860–867. <https://doi.org/10.1016/j.cub.2017.01.058>.
40. Edgar, L.G., and Goldstein, B. (2012). Culture and manipulation of embryonic cells. *Method Cell Biol.* 107, 151–175. <https://doi.org/10.1016/b978-0-12-394620-1.00005-9>.
41. Hertwig, O. (1893). Ueber den Werth der ersten Furchungszellen für die Organbildung des Embryo Experimentelle Studien am Frosch- und Tritonei. *Archiv f. mikrosk. Anat.* 42, 662–807. <https://doi.org/10.1007/bf02976796>.
42. O’Connell, C.B., and Wang, Y.L. (2000). Mammalian spindle orientation and position respond to changes in cell shape in a dynein-dependent fashion. *Mol. Biol. Cell* 11, 1765–1774. <https://doi.org/10.1091/mbc.11.5.1765>.

43. Minc, N., Burgess, D., and Chang, F. (2011). Influence of cell geometry on division-plane positioning. *Cell* 144, 414–426. <https://doi.org/10.1016/j.cell.2011.01.016>.
44. Chen, D., Hastie, E., and Sherwood, D. (2019). Endogenous expression of UNC-59/Septin in *C. elegans*. *MicroPubl. Biol.* 2019. <https://doi.org/10.17912/micropub.biology.000200>.
45. Heppert, J.K., Dickinson, D.J., Pani, A.M., Higgins, C.D., Steward, A., Ahringer, J., Kuhn, J.R., and Goldstein, B. (2016). Comparative assessment of fluorescent proteins for *in vivo* imaging in an animal model system. *Mol. Biol. Cell* 27, 3385–3394. <https://doi.org/10.1091/mbc.E16-01-0063>.
46. Kachur, T.M., Audhya, A., and Pilgrim, D.B. (2008). UNC-45 is required for NMY-2 contractile function in early embryonic polarity establishment and germline cellularization in *C. elegans*. *Dev. Biol.* 314, 287–299. <https://doi.org/10.1016/j.ydbio.2007.11.028>.
47. Larson, M.E., and Bement, W.M. (2017). Automated mitotic spindle tracking suggests a link between spindle dynamics, spindle orientation, and anaphase onset in epithelial cells. *Mol. Biol. Cell* 28, 746–759. <https://doi.org/10.1091/mbc.E16-06-0355>.
48. Strauss, B., Adams, R.J., and Papalopulu, N. (2006). A default mechanism of spindle orientation based on cell shape is sufficient to generate cell fate diversity in polarised *Xenopus* blastomeres. *Development* 133, 3883–3893. <https://doi.org/10.1242/dev.02578>.
49. Rose, L., and Gönczy, P. (2014). Polarity establishment, asymmetric division and segregation of fate determinants in early *C. elegans* embryos. *WormBook*, 1–43. <https://doi.org/10.1895/wormbook.1.30.2>.
50. Nishimura, K., Fukagawa, T., Takisawa, H., Kakimoto, T., and Kanemaki, M. (2009). An auxin-based degron system for the rapid depletion of proteins in nonplant cells. *Nat. Methods* 6, 917–922. <https://doi.org/10.1038/nmeth.1401>.
51. Zhang, L., Ward, J.D., Cheng, Z., and Dernburg, A.F. (2015). The auxin-inducible degradation (AID) system enables versatile conditional protein depletion in *C. elegans*. *Development* 142, 4374–4384. <https://doi.org/10.1242/dev.129635>.
52. Gotta, M., Dong, Y., Peterson, Y.K., Lanier, S.M., and Ahringer, J. (2003). Asymmetrically Distributed *C. elegans* Homologs of AGS3/PINS Control Spindle Position in the Early Embryo. *Curr. Biol.* 13, 1029–1037. [https://doi.org/10.1016/S0960-9822\(03\)00371-3](https://doi.org/10.1016/S0960-9822(03)00371-3).
53. Srinivasan, D.G., Fisk, R.M., Xu, H., and van den Heuvel, S. (2003). A complex of LIN-5 and GPR proteins regulates G protein signaling and spindle function in *C. elegans*. *Genes Dev.* 17, 1225–1239. <https://doi.org/10.1101/gad.1081203>.
54. Fox, P.M., and Schedl, T. (2015). Analysis of Germline Stem Cell Differentiation Following Loss of GLP-1 Notch Activity in *Caenorhabditis elegans*. *Genetics* 207, 167–184. <https://doi.org/10.1534/genetics.115.178061>.
55. Kotak, S. (2019). Mechanisms of Spindle Positioning: Lessons from Worms and Mammalian Cells. *Biomolecules* 9, 80. <https://doi.org/10.3390/biom9020080>.
56. Tanenbaum, M.E., and Medema, R.H. (2010). Mechanisms of Centrosome Separation and Bipolar Spindle Assembly. *Dev. Cell* 19, 797–806. <https://doi.org/10.1016/j.devcel.2010.11.011>.
57. Zhou, K., Rolls, M.M., Hall, D.H., Malone, C.J., and Hanna-Rose, W. (2009). A ZYG-12-dynein interaction at the nuclear envelope defines cytoskeletal architecture in the *C. elegans* gonad. *J. Cell Biol.* 186, 229–241. <https://doi.org/10.1083/jcb.200902101>.
58. Strome, S. (1993). Determination of cleavage planes. *Cell* 72, 3–6. [https://doi.org/10.1016/0092-8674\(93\)90041-n](https://doi.org/10.1016/0092-8674(93)90041-n).
59. Yamashita, Y.M., Mahowald, A.P., Perlin, J.R., and Fuller, M.T. (2007). Asymmetric inheritance of mother versus daughter centrosome in stem cell division. *Science* 315, 518–521. <https://doi.org/10.1126/science.1134910>.
60. Rebollo, E., Sampaio, P., Januschke, J., Llamazares, S., Varmark, H., and González, C. (2007). Functionally unequal centrosomes drive spindle orientation in asymmetrically dividing *Drosophila* neural stem cells. *Dev. Cell* 12, 467–474. <https://doi.org/10.1016/j.devcel.2007.01.021>.
61. Rusan, N.M., and Peifer, M. (2007). A role for a novel centrosome cycle in asymmetric cell division. *J. Cell Biol.* 177, 13–20. <https://doi.org/10.1083/jcb.200612140>.
62. Hyman, A.A., and White, J.G. (1987). Determination of cell division axes in the early embryogenesis of *Caenorhabditis elegans*. *J. Cell Biol.* 105, 2123–2135. <https://doi.org/10.1083/jcb.105.5.2123>.
63. Kotak, S., Busso, C., and Gönczy, P. (2013). NuMA phosphorylation by CDK1 couples mitotic progression with cortical dynein function. *EMBO J.* 32, 2517–2529. <https://doi.org/10.1038/emboj.2013.172>.
64. Zheng, Z., Wan, Q., Meixiong, G., and Du, Q. (2014). Cell cycle-regulated membrane binding of NuMA contributes to efficient anaphase chromosome separation. *Mol. Biol. Cell* 25, 606–619. <https://doi.org/10.1091/mbc.E13-08-0474>.
65. Portegijs, V., Fielmich, L.E., Galli, M., Schmidt, R., Muñoz, J., van Mourik, T., Akhmanova, A., Heck, A.J.R., Boxem, M., and van den Heuvel, S. (2016). Multisite Phosphorylation of NuMA-Related LIN-5 Controls Mitotic Spindle Positioning in *C. elegans*. *PLoS Genet.* 12, e1006291. <https://doi.org/10.1371/journal.pgen.1006291>.
66. Sana, S., Keshri, R., Rajeevan, A., Kapoor, S., and Kotak, S. (2018). Plk1 regulates spindle orientation by phosphorylating NuMA in human cells. *Life Sci. Alliance* 1, e201800223. <https://doi.org/10.26508/lsa.201800223>.
67. Kotak, S., Afshar, K., Busso, C., and Gönczy, P. (2016). Aurora A kinase regulates proper spindle positioning in *C. elegans* and in human cells. *J. Cell Sci.* 129, 3015–3025. <https://doi.org/10.1242/jcs.184416>.
68. Gallini, S., Carminati, M., De Mattia, F., Pirovano, L., Martini, E., Oldani, A., Asteriti, I.A., Guarguaglini, G., and Mapelli, M. (2016). NuMA Phosphorylation by Aurora-A Orchestrates Spindle Orientation. *Curr. Biol.* 26, 458–469. <https://doi.org/10.1016/j.cub.2015.12.051>.
69. Kelkar, M., Bohec, P., Smith, M.B., Sreenivasan, V., Lisica, A., Valon, L., Ferber, E., Baum, B., Salbreux, G., and Charras, G. (2022). Spindle reorientation in response to mechanical stress is an emergent property of the spindle positioning mechanisms. *Proc. Natl. Acad. Sci. USA* 119, e2121868119. <https://doi.org/10.1073/pnas.2121868119>.
70. Okumura, M., Natsume, T., Kanemaki, M.T., and Kiyomitsu, T. (2018). Dynein-Dynactin-NuMA clusters generate cortical spindle-pulling forces as a multi-arm ensemble. *Elife* 7, e36559. <https://doi.org/10.7554/eLife.36559>.
71. Anjur-Dietrich, M.I., Gomez Hererra, V., Farhadifar, R., Wu, H., Merta, H., Bahmanyar, S., Shelley, M.J., and Needleman, D.J. (2024). Mechanics of spindle orientation in human mitotic cells is determined by pulling forces on astral microtubules and clustering of cortical dynein. *Dev. Cell* 59, 2429–2442.e4. <https://doi.org/10.1016/j.devcel.2024.05.022>.
72. Schmidt, R., Fielmich, L.E., Grigoriev, I., Katrukha, E.A., Akhmanova, A., and van den Heuvel, S. (2017). Two populations of cytoplasmic dynein contribute to spindle positioning in *C. elegans* embryos. *J. Cell Biol.* 216, 2777–2793. <https://doi.org/10.1083/jcb.201607038>.
73. Sheeman, B., Carvalho, P., Sagot, I., Geiser, J., Kho, D., Hoyt, M.A., and Pellman, D. (2003). Determinants of *S. cerevisiae* dynein localization and activation: implications for the mechanism of spindle positioning. *Curr. Biol.* 13, 364–372. [https://doi.org/10.1016/s0960-9822\(03\)00013-7](https://doi.org/10.1016/s0960-9822(03)00013-7).
74. Siegrist, S.E., and Doe, C.Q. (2005). Microtubule-induced Pins/Galphi cortical polarity in *Drosophila* neuroblasts. *Cell* 123, 1323–1335. <https://doi.org/10.1016/j.cell.2005.09.043>.
75. Zheng, Z., Wan, Q., Liu, J., Zhu, H., Chu, X., and Du, Q. (2013). Evidence for dynein and astral microtubule-mediated cortical release and transport of Galphi/LGN/NuMA complex in mitotic cells. *Mol. Biol. Cell* 24, 901–913. <https://doi.org/10.1091/mbc.E12-06-0458>.
76. Tame, M.A., Raaijmakers, J.A., van den Broek, B., Lindqvist, A., Jalink, K., and Medema, R.H. (2014). Astral microtubules control redistribution of dynein at the cell cortex to facilitate spindle positioning. *Cell Cycle* 13, 1162–1170. <https://doi.org/10.4161/cc.28031>.

77. Bergstralh, D.T., Lovegrove, H.E., and St Johnston, D. (2015). Lateral adhesion drives reintegration of misplaced cells into epithelial monolayers. *Nat. Cell Biol.* *17*, 1497–1503. <https://doi.org/10.1038/ncb3248>.
78. Zhou, Z., Alégot, H., and Irvine, K.D. (2019). Oriented Cell Divisions Are Not Required for Drosophila Wing Shape. *Curr. Biol.* *29*, 856–864.e853. <https://doi.org/10.1016/j.cub.2019.01.044>.
79. Kamath, R.S., Fraser, A.G., Dong, Y., Poulin, G., Durbin, R., Gotta, M., Kanapin, A., Le Bot, N., Moreno, S., Sohrmann, M., et al. (2003). Systematic functional analysis of the *Caenorhabditis elegans* genome using RNAi. *Nature* *421*, 231–237. <https://doi.org/10.1038/nature01278>.
80. Goupil, E., Amini, R., Hall, D.H., and Labbé, J.C. (2017). Actomyosin contractility regulators stabilize the cytoplasmic bridge between the two primordial germ cells during *Caenorhabditis elegans* embryogenesis. *Mol. Biol. Cell* *28*, 3789–3800. <https://doi.org/10.1091/mbc.E17-08-0502>.
81. Pekar, O., Ow, M.C., Hui, K.Y., Noyes, M.B., Hall, S.E., and Hubbard, E.J.A. (2017). Linking the environment, DAF-7/TGF β signaling and LAG-2/DSL ligand expression in the germline stem cell niche. *Development* *144*, 2896–2906. <https://doi.org/10.1242/dev.147660>.
82. McNally, K., Audhya, A., Oegema, K., and McNally, F.J. (2006). Katanin controls mitotic and meiotic spindle length. *J. Cell Biol.* *175*, 881–891. <https://doi.org/10.1083/jcb.200608117>.
83. Oegema, K., Desai, A., Rybina, S., Kirkham, M., and Hyman, A.A. (2001). Functional Analysis of Kinetochore Assembly in *Caenorhabditis elegans*. *J. Cell Biol.* *153*, 1209–1226. <https://doi.org/10.1083/jcb.153.6.1209>.
84. Strome, S., Powers, J., Dunn, M., Reese, K., Malone, C.J., White, J., Seydoux, G., and Saxton, W. (2001). Spindle dynamics and the role of gamma-tubulin in early *Caenorhabditis elegans* embryos. *Mol. Biol. Cell* *12*, 1751–1764. <https://doi.org/10.1091/mbc.12.6.1751>.
85. Mangal, S., Sacher, J., Kim, T., Osório, D.S., Motegi, F., Carvalho, A.X., Oegema, K., and Zanin, E. (2018). TPXL-1 activates Aurora A to clear contractile ring components from the polar cortex during cytokinesis. *J. Cell Biol.* *217*, 837–848. <https://doi.org/10.1083/jcb.201706021>.
86. Heppert, J.K., Pani, A.M., Roberts, A.M., Dickinson, D.J., and Goldstein, B. (2018). A CRISPR Tagging-Based Screen Reveals Localized Players in Wnt-Directed Asymmetric Cell Division. *Genetics* *208*, 1147–1164. <https://doi.org/10.1534/genetics.117.300487>.
87. Ihara, S. (2021). N-terminally endogenous mKate2-tagged HIM-4 in *Caenorhabditis elegans*. *MicroPubl. Biol.* *2021*. <https://doi.org/10.17912/micropub.biology.000386>.
88. Ashley, G.E., Duong, T., Levenson, M.T., Martinez, M.A.Q., Johnson, L.C., Hibshman, J.D., Saeger, H.N., Palmisano, N.J., Doonan, R., Martinez-Mendez, R., et al. (2021). An expanded auxin-inducible degron toolkit for *Caenorhabditis elegans*. *Genetics* *217*, iyab006. <https://doi.org/10.1093/genetics/iyab006>.
89. Cheng, E., Lu, R., and Gerhold, A.R. (2024). Non-autonomous insulin signaling delays mitotic progression in *C. elegans* germline stem and progenitor cells. *PLoS Genet.* *20*, e1011351. <https://doi.org/10.1371/journal.pgen.1011351>.
90. Timmons, L., and Fire, A. (1998). Specific interference by ingested dsRNA. *Nature* *395*, 854. <https://doi.org/10.1038/27579>.
91. Natsume, T., Kiyomitsu, T., Saga, Y., and Kanemaki, M.T. (2016). Rapid Protein Depletion in Human Cells by Auxin-Inducible Degron Tagging with Short Homology Donors. *Cell Rep.* *15*, 210–218. <https://doi.org/10.1016/j.celrep.2016.03.001>.
92. Dickinson, D.J., Pani, A.M., Heppert, J.K., Higgins, C.D., and Goldstein, B. (2015). Streamlined Genome Engineering with a Self-Excising Drug Selection Cassette. *Genetics* *200*, 1035–1049. <https://doi.org/10.1534/genetics.115.178335>.
93. Schindelin, J., Arganda-Carreras, I., Frise, E., Kaynig, V., Longair, M., Pietzsch, T., Preibisch, S., Rueden, C., Saalfeld, S., Schmid, B., et al. (2012). Fiji: an open-source platform for biological-image analysis. *Nat. Methods* *9*, 676–682. <https://doi.org/10.1038/nmeth.2019>.
94. The MathWorks Inc. (2020) MATLAB Version: 9.9.0 (R2020b).
95. Tinevez, J.-Y., Perry, N., Schindelin, J., Hoopes, G.M., Reynolds, G.D., Laplantine, E., Bednarek, S.Y., Shorte, S.L., and Eliceiri, K.W. (2017). TrackMate: An open and extensible platform for single-particle tracking. *Methods* *115*, 80–90. <https://doi.org/10.1016/j.ymeth.2016.09.016>.
96. Oxford Instruments (2018). Imapris9.2.1.
97. Bezanson, J., Edelman, A., Karpinski, S., and Shah, V.B. (2017). Julia: A Fresh Approach to Numerical Computing. *SIAM Review* *59*, 65–98. <https://doi.org/10.1137/141000671>.
98. Van Rossum, G., and Drake, F.L. (2009). *Python 3 Reference Manual (CreateSpace)*.
99. Gerhold, A.R., Ryan, J., Vallée-Trudeau, J.N., Dorn, J.F., Labbé, J.C., and Maddox, P.S. (2015). Investigating the regulation of stem and progenitor cell mitotic progression by in situ imaging. *Curr. Biol.* *25*, 1123–1134. <https://doi.org/10.1016/j.cub.2015.02.054>.
100. Brenner, S. (1974). The genetics of *Caenorhabditis elegans*. *Genetics* *77*, 71–94. <https://doi.org/10.1093/genetics/77.1.71>.
101. Stiernagle, T. (2006). Maintenance of *C. elegans*. In *WormBook: The Online Review of C. elegans Biology [Internet] (WormBook)*.
102. Dickinson, D.J., Ward, J.D., Reiner, D.J., and Goldstein, B. (2013). Engineering the *Caenorhabditis elegans* genome using Cas9-triggered homologous recombination. *Nat. Methods* *10*, 1028–1034. <https://doi.org/10.1038/nmeth.2641>.
103. Huang, G., de Jesus, B., Koh, A., Blanco, S., Rettmann, A., DeMott, E., Sylvester, M., Ren, C., Meng, C., Waterland, S., et al. (2021). Improved CRISPR/Cas9 knock-in efficiency via the self-excising cassette (SEC) selection method in *C. elegans*. *MicroPubl. Biol.* *2021*. <https://doi.org/10.17912/micropub.biology.000460>.
104. Frokjaer-Jensen, C., Davis, M.W., Hopkins, C.E., Newman, B.J., Thummel, J.M., Olesen, S.P., Grunnet, M., and Jorgensen, E.M. (2008). Single-copy insertion of transgenes in *Caenorhabditis elegans*. *Nat. Genet.* *40*, 1375–1383. <https://doi.org/10.1038/ng.248>.
105. Juschke, C., Xie, Y., Postiglione, M.P., and Knoblich, J.A. (2014). Analysis and modeling of mitotic spindle orientations in three dimensions. *Proc. Natl. Acad. Sci. USA* *111*, 1014–1019. <https://doi.org/10.1073/pnas.1314984111>.
106. Fachada, N., and C. Rosa, A. (2018). micompm: A MATLAB/Octave toolbox for multivariate independent comparison of observations. *J. Open Source Softw.* *3*, 430. <https://doi.org/10.21105/joss.00430>.

STAR★METHODS

KEY RESOURCES TABLE

REAGENT or RESOURCE	SOURCE	IDENTIFIER
Bacterial and virus strains		
<i>Escherichia coli</i> OP50	Caenorhabditis Genetics Center (CGC)	OP50
<i>Escherichia coli</i> HT115(DE3)	CGC	HT115(DE3)
Ahringer RNAi Library	Source Bioscience	<i>C. elegans</i> RNAi Collection (Ahringer) ⁷⁹
Chemicals, peptides, and recombinant proteins		
Tetramisole	Sigma	Cat #L9756
Auxin indole-3-acetic acid (IAA)	Sigma	Cat #I3750
Inulin from chicory	Sigma	Cat #I2255
HEPES/Hepes	Wisent	Cat #600-032-CG
Leibovitz L-15 1X with L-Glutamine without Sodium Bicarbonate	Wisent	Cat #323-050-CL
Fetal Bovine Serum (FBS)	Wisent	Cat #090–150, lot 112740
Experimental models: Organisms/strains		
<i>C. elegans</i> : Strain N2; genotype: N2 Bristol	CGC	N2
<i>C. elegans</i> : Strain UM227; genotype: <i>ItIs38</i> [<i>pAA1</i> ; <i>pie-1::GFP::PH(PLC1delta1)</i> ; <i>unc-119(+)</i>] III	Goupil et al. ⁸⁰	UM227
<i>C. elegans</i> : Strain UM537; genotype: <i>nals37</i> [<i>pGC457(Plag-2::PHdomain::mCherry-unc119(+))</i> ; <i>tnIs6[lim-7::GFP + rol-6(su1006)]</i>]	This study. Allele/transgene source(s): Hall et al. ³⁰ ; Pekar et al. ⁸¹	UM537
<i>C. elegans</i> : Strain UM563; genotype: <i>ItIs37</i> [<i>pAA64</i> ; <i>pie-1::mCherry::HIS-58</i> ; <i>unc-119(+)</i>]IV; <i>ddIs6[tbg-1::GFP + unc-119(+)]V</i>	This study. Allele/transgene source(s): McNally et al. ⁸² ; Oegema et al. ⁸³	UM563
<i>C. elegans</i> : Strain UM679; genotype: <i>ItSi567</i> [<i>pOD1517/pSW222</i> ; <i>Pmex-5::mCherry::tbb-2::tbb-2_3'UTR</i> ; <i>cb-unc-119(+)</i>] I; <i>ani-1(mon7)</i> [<i>mNeonGreen</i> 3xFlag:: <i>ani-1</i>] III	Zellag et al. ³⁷	UM679
<i>C. elegans</i> : Strain UM792; genotype: <i>cpSi20</i> [<i>Pmex-5::TAGRFPT::PH::tbb-2_3'UTR + unc-119 (+)</i>] II; <i>ani-1(mon7)</i> [<i>mNeonGreen</i> 3xFlag:: <i>ani-1</i>] III; <i>ojIs1</i> [<i>unc-119(+)</i> <i>pie-1::GFP::tbb-2</i>] V	This study. Allele/transgene source(s): Rehai-Bell et al. ³⁹ ; Heppert et al. ⁴⁵ ; Strome et al. ⁸⁴	UM792
<i>C. elegans</i> : Strain UM793; genotype: <i>unc-59(qy50)</i> [<i>unc-59::GFP::3xflag::AID</i>] I; <i>cpSi20</i> [<i>Pmex-5::TAGRFPT::PH::tbb-2_3'UTR + unc-119 (+)</i>] II; <i>ojIs1</i> [<i>unc-119(+)</i> <i>pie-1::GFP::tbb-2</i>] V	This study. Allele/transgene source(s): Chen et al. ⁴⁴ ; Heppert et al. ⁴⁵ ; Strome et al. ⁸⁴	UM793
<i>C. elegans</i> : Strain UM796; genotype: <i>lin-5(cp288)</i> [<i>lin-5::mNG-C1</i> 3xFlag] II; ; <i>estSi57</i> [<i>pEZ152</i> ; <i>pani-1::mKate2::ANI-1</i> ; <i>cb-unc-119(+)</i>] IV	This study. Allele/transgene source(s): Mangal et al. ⁸⁵ ; Heppert et al. ⁸⁶	UM796
<i>C. elegans</i> : Strain UM798; genotype: <i>dhc-1</i> (i.e.,28[<i>dhc-1::degron::GFP</i>]) <i>ItSi567</i> [<i>pOD1517/pSW222</i> ; <i>Pmex-5::mCherry::tbb-2::tbb-2_3'UTR</i> ; <i>cb-unc-119(+)</i>] I; <i>ieSi38</i> [<i>sun-1p::TIR-1::mRuby::sun-1_3'UTR + Cbr-unc-119(+)</i>] IV	This study. Allele/transgene source(s): Zhang et al. ⁵¹	UM798

(Continued on next page)

Continued

REAGENT or RESOURCE	SOURCE	IDENTIFIER
<i>C. elegans</i> : Strain UM799 ; genotype: <i>lin-5(cp288[lin-5::mNG-C1'3xFlag] II; lts44[pAA173, pie-1p-mCherry::PH(PLC1delta1)V + unc-119(+)]</i>	This study. Allele/transgene source(s): Kachur et al. ⁴⁶ ; Heppert et al. ⁸⁶	UM799
<i>C. elegans</i> : Strain UM801 ; genotype: <i>dhc-1(i.e.,28[dhc-1::degron::GFP]) ItSi567[pOD1517/pSW222; Pmex-5::mCherry::tbb-2::tbb-2_3'UTR; cb-unc-119(+)] I; ieSi38[sun-1p::TIR-1::mRuby::sun-1 3'UTR + Cbr-unc-119(+)] IV; xyz18[mkate2::HIM-4] X</i>	This study. Allele/transgene source(s): Zhang et al. ⁵¹ ; Ihara ⁸⁷	UM801
<i>C. elegans</i> : Strain UM802 ; genotype: <i>dhc-1(i.e.,28[dhc-1::degron::GFP]) ItSi567[pOD1517/pSW222; Pmex-5::mCherry::tbb-2::tbb-2_3'UTR; cb-unc-119(+)] I; cpSi20[Pmex-5::TAGRFPT::PH::tbb-2 3'UTR + unc-119(+)] II; ieSi38[sun-1p::TIR-1::mRuby::sun-1 3'UTR + Cbr-unc-119(+)] IV</i>	This study. Allele/transgene source(s): Heppert et al. ⁴⁵ ; Zhang et al. ⁵¹	UM802
<i>C. elegans</i> : Strain UM805; genotype: <i>ItSi567[pOD1517/pSW222; Pmex-5::mCherry::tbb-2::tbb-2_3'UTR; cb-unc-119(+)] I; lin-5(os205[lin-5::mAID::mNG] II; ieSi38[sun-1p::TIR-1::mRuby::sun-1 3'UTR + Cbr-unc-119(+)] IV</i>	This study. Allele/transgene source(s): Zhang et al. ⁵¹	UM805
<i>C. elegans</i> : Strain UM806; genotype: <i>wrdSi50[mex-5p::TIR1::F2A::mTagBFP2::AID*::NLS::tbb-2 3'UTR] I; lin-5(os205[lin-5::mAID::mNG] II; estSi57[pEZ152; pani-1::mKate2::ANI-1; cb-unc-119(+)] IV</i>	This study. Allele/transgene source(s): Mangal et al. ⁸⁵ ; Ashley et al. ⁸⁸	UM806
<i>C. elegans</i> : Strain UM808; genotype: <i>lin-5(os205[lin-5::mAID::mNG] II; ieSi38[sun-1p::TIR-1::mRuby::sun-1 3'UTR + Cbr-unc-119(+)] IV; lts38 [pAA1; pie-1::GFP::PH(PLC1delta1); unc-119(+)] III</i>	This study. Allele/transgene source(s): Zhang et al. ⁵¹ ; Goupil et al. ⁸⁰	UM808
<i>C. elegans</i> : Strain JDU19; genotype: <i>ijmSi7 [pJD348/pSW077; mosl_5'mex-5_GFP::tbb-2; mCherry::his-11; cb-unc-119(+)] I; unc-119(ed3) III</i>	Benjamin Lacroix	JDU19
<i>C. elegans</i> : Strain ARG3; genotype: <i>ItSi567 [pOD1517/pSW222; Pmex-5::mCherry::tbb-2::tbb-2_3'UTR; cb-unc-119(+)] I</i>	Cheng et al. ⁸⁹	ARG3
<i>C. elegans</i> : Strain ARG50; genotype: <i>ijmSi7 [pJD348/pSW077; mosl_5'mex-5_GFP::tbb-2; mCherry::his-11; cb-unc-119(+)] I</i>	Cheng et al. ⁸⁹	ARG50
<i>C. elegans</i> : Strain ARG59; genotype: <i>ItSi567[pOD1517/pSW222; Pmex-5::mCherry::tbb-2::tbb-2_3'UTR; cb-unc-119(+)] I; unc-119(ed3) III; ieSi38[sun-1p::TIR-1::mRuby::sun-1 3'UTR + Cbr-unc-119(+)] IV</i>	Cheng et al. ⁸⁹	ARG59
<i>C. elegans</i> : Strain NK2446; genotype: <i>lam-2(qy41[lam-2::mKate2]) X</i>	CGC	NK2446

(Continued on next page)

Continued		
REAGENT or RESOURCE	SOURCE	IDENTIFIER
<i>C. elegans</i> : Strain HS3911; genotype: <i>lin-5(os205[lin-5::mAID::mNG] II</i>	This study	HS3911
<i>C. elegans</i> : Strain PD1594; genotype: <i>ccTi1594 [mex-5p::GFP::gpr-1::smu-1 3' UTR + Cbr-unc-119(+), III: 680195] III</i>	CGC	PD1594
Oligonucleotides		
Guide RNA sequence for generating LIN-5:mAID:mNG: 5'-GTCCAAGAAAAGAA CCGTC-3'	Heppert et al. ⁸⁶	N/A
Primers for generating LIN-5:mAID:mNG, see Table S1	This study	N/A
Recombinant DNA		
L4440 (RNAi empty vector for feeding)	Timmons and Fire ⁹⁰	RRID: Addgene_1654
<i>gpr-1/2</i> feeding RNAi	Kamath et al. ⁷⁹	sjj_C38C10.4
mAID-mClover-Hygro	Natsume et al. ⁹¹	RRID: Addgene_72828
mNG-mom-5	Heppert et al. ⁸⁶	
mKate2 ² SEC ³ xMyc	Dickinson et al. ⁹²	RRID: Addgene_70685
<i>lin-5:mAID:mNG</i>	This study	pTN26
Software and algorithms		
Fiji 1.52v	Schindelin et al. ⁹³	Fiji (RRID:SCR_002285)
MATLAB 2020b	MathWorks ⁹⁴	MATLAB (RRID:SCR_001622)
Trackmate 6.0.0	Tinevez et al. ⁹⁵	https://imagej.net/plugins/trackmate/
Imaris 9.2.1	Oxford Instruments ⁹⁶	Imaris (RRID:SCR_007370)
Julia 1.10.4	Bezanson et al. ⁹⁷	Julia Programming Language (RRID:SCR_021666)
Python 3	Van Rossum and Drake ⁹⁸	Python Programming Language (RRID:SCR_008394)
Custom scripts	This study	https://github.com/VincentPoupart/Zellag2024
CentTracker scripts	Zellag et al. ³⁷	https://github.com/yifnzha0/CentTracker
Other		
Microfabricated silica wafer	Zellag et al. ^{37,38} ; Gerhold et al. ⁹⁹	N/A
Glass slides with wells for gonad explant culture and imaging	Fisher Scientific	30-2066A-BROWN 3 SQUARE 14mm with Bars Epoxy autoclavable

EXPERIMENTAL MODEL AND STUDY PARTICIPANT DETAILS

C. elegans strain maintenance

C. elegans animals were maintained at 20°C on nematode growth medium (NGM) and fed with *Escherichia coli* strain OP50 according to standard protocols.¹⁰⁰ All strains used in this study are listed in the [key resources table](#). For all experiments, late L4 stage hermaphrodite animals were identified by size and vulva morphology and individually collected from these plates, except for the dataset of [Figure 1](#), where different developmental stages were obtained by synchronizing larvae at the L1 stage. Synchronized L1 larvae were obtained by sodium hypochlorite treatment.¹⁰¹ Briefly, gravid hermaphrodites were dissolved in a solution of 1.2% sodium hypochlorite and 250 mM sodium hydroxide. Pelleted embryos were washed 3 times in M9 buffer (22.04 mM KH₂PO₄, 42.27 mM Na₂HPO₄, 85.55 mM NaCl, 1 mM MgSO₄), and allowed to hatch for 24 h at 15°C in M9 buffer. Animals at the L3, late L4 and adult day 1 stages were obtained by inoculation of synchronized L1 larvae on NGM plates containing 1 mM isopropyl β-D-thiogalactoside and 25 μg/mL carbenicillin and fed for respectively 26–30, 40–48 and 72 h with *E. coli* strain HT115 transformed with the empty RNA interference (RNAi) vector L4440. The strains used in this study are listed in the [key resources table](#).

METHOD DETAILS

Generation of mAID:mNG-tagged LIN-5

The plasmid used for tagging *lin-5* with mNeonGreen (mNG) and mAID was constructed as follows. Homology arms in the coding sequence of *lin-5* and in the 3'-UTR region were amplified using genomic DNA as a template. mAID was amplified from the plasmid pMK290 (Natsume et al.⁹¹; Addgene: #72828). mNG was amplified from a plasmid containing *mNG-mom-5*.⁸⁶ The self-excising cassette (SEC) was amplified from the plasmid pDD287 (Dickinson et al.⁹², Addgene #70685). The plasmid backbone was amplified from the pDD287 plasmid. These fragments were assembled using NEBuilder to construct the donor plasmid, pTN26 (*lin-5::mAID::mNG*). For Cas9 and sgRNA expression, a guide RNA sequence (5'-GTCCAAGAAAAGAACCGTC-3') targeting the C-terminal coding region of the *lin-5* gene was used, as in Heppert et al.⁸⁶ The plasmid, pTN27 (sg *lin-5*), was constructed by inverse PCR with the plasmid pDD162 (Dickinson et al.¹⁰², Addgene #47549). Editing of the *lin-5* locus was performed as described previously.¹⁰³ Briefly, 25 ng/μL of pTN26 and 5 ng/μL of pTN27 were injected into the gonad of N2 animals with the control injection markers pCFJ90 (*Pmyo-2::mCherry*, Addgene #8984, Frokjaer-Jensen et al.¹⁰⁴) and pCFJ104 (*Pmyo-3::mCherry*, Addgene #19328, Frokjaer-Jensen et al.¹⁰⁴). The site of mAID:mNG insertion was verified by PCR on the genomic DNA of homozygous progeny. All oligonucleotide sequences are reported in the [key resources table](#) or [Table S1](#).

Worm mounting and live imaging

Animals were anesthetized in M9 buffer containing 0.04% tetramisole (Sigma, Cat #L9756) and transferred to a 3% agarose pad, molded with grooves made by a custom microfabricated silica plate, as described previously.^{37,38,99} A glass coverslip was placed onto the pad, the chamber was backfilled with M9 buffer containing 0.04% tetramisole and sealed using VaLaP (1:1:1 Vaseline, Lanolin, and Paraffin). Images were acquired at room temperature (~20°C) on either a Zeiss Cell Observer spinning disk confocal microscope (Zeiss inverted Cell Observer with a Yokogawa CSU-X1 confocal scanner, controlled by Zen software, using a Zeiss 63x/1.4 NA Plan Apochromat DIC (UV) VIS-IR oil immersion objective, 488 nm (30mW) and 561 nm (50mW) solid-state lasers, with a quad pass 466/523/600/677 emission filter and a Zeiss AxioCam 506 Mono camera) or a Nikon CSU-X1 spinning disk confocal microscope (Nikon Ti2-E inverted microscope with a Yokogawa CSU-X1 confocal scanner, controlled by NIS-Elements software, using either a Nikon Plan Apo Lambda 60x/1.4 NA Oil immersion objective or a Nikon Apo 40x/1.25 NA water immersion objective, 488 nm (100mW) and 561 nm (100mW) solid-state lasers, with a dual band pass Chroma 59004m filter or single pass filters EM525/50, EM605/55, EM700/75, and a Hamamatsu ORCA-Fusion BT sCMOS camera). Detailed imaging conditions are reported in [Table S2](#).

Auxin treatment

A 400 mM Auxin stock in ethanol was prepared from natural auxin indole-3-acetic acid (IAA, Sigma Cat #I3750) as described in Zhang et al.⁵¹ Auxin was added at final concentration of 1mM to the NGM solution before pouring plates. Plates were inoculated with OP50 and left at room temperature in the dark for 2 days before use. L4 stage animals were collected from OP50 seeded NGM plates, washed in 100 μL of M9 buffer and then transferred to OP50 seeded NGM-Auxin plates for either 40 min or 6 h at room temperature in the dark prior to mounting and imaging. The level of depletion was quantified by measuring the mean fluorescence intensity of DHC-1::AID::GFP and LIN-5::mAID:mNG in control and AID-treated animals in Fiji 1.52v.⁹³ Three ~200 μm² rectangles were drawn manually across the mitotic region of the gonad and the average intensity was measured in 3 z-slices around the middle of the gonad. Measurements are reported as the mean value per gonad after autofluorescence was subtracted. Autofluorescence was measured using the same approach but on gonads from animals carrying only mCH:β-tubulin (strain ARG3).

RNAi treatment

RNAi was performed by feeding. HT115 with the *gpr-1/2* or L4440 (empty vector) plasmid were grown for 12–16 h in LB + 100 μg/mL ampicillin (LB/Amp) at 37°C with shaking. This culture was diluted 1:100 in 25 mL of LB/Amp and grown for 6 h under the same conditions. 6 h cultures were pelleted by centrifugation at 4000 rcf for 5 min and resuspended in 0.5 mL LB. 50 μL of resuspended bacteria was added per 35 mm NGM/IPTG/Carb plate (NGM with 1 mM isopropyl β-d-thiogalactoside (IPTG) and 50 μg/mL carbenicillin). Seeded plates were kept in the dark, at room temperature for 1 day. Synchronized larvae were obtained by egg collection directly on RNAi plates, and L4 larvae were selected ~3 days later for live-cell imaging.

Gonad explants

Three L4 stage larvae, raised on OP50-seeded NGM plates, were transferred into a ~5 μL drop of meiosis medium (0.5 mg/mL Inulin (Sigma, Cat #I2255), 25 mM HEPES pH 7.5 (Wisent, Cat #600-032-CG), 60% Leibovitz's L-15 Media (Wisent, Cat #323-050-CL), 20% FBS heat inactivated (Wisent, Cat #090-150, lot 112740)),⁴⁰ on a glass slide patterned with 14 mm × 14 mm wells (Fisher Scientific, 30-2066A-BROWN 3 SQUARE 14mm with Bars Epoxy autoclavable). Using 25-gauge needles (BD Precision Glide #CABD305122), animals were cut below the pharynx, extruding at least one gonad arm into the medium. A coverslip was then gently placed over the drop and sealed with VaLaP. With this method, ~1/3 of explants remained intact, as assessed by germ line morphology, and were kept for time-lapse imaging.

Germ cell centrosome tracking and scoring of mitotic events

Image registration, centrosome tracking and pairing, and scoring of mitotic events (e.g., nuclear envelop breakdown (NEBD)) were performed using CentTracker, as described previously.^{37,38} Briefly, z stack images were registered to correct for sample movement over time. Centrosomes were tracked in Fiji 1.52v⁹³ using the plug-in TrackMate v6.0.0⁹⁵ and their x-y-z-t coordinates were processed using a trainable, machine-learning-based approach to retain true pairs of centrosomes (captures ~70% of centrosome pairs per germ line in wild-type conditions). For experiments other than those in Figure 1, the true pair processing step was done manually to retain the maximum number of centrosome pairs possible (close to 100% per germ line). The centrosome-to-centrosome distance (spindle length) overtime was then used to define four mitotic events: the start of centrosome separation in prophase, NEBD, prometaphase-metaphase, and anaphase onset, as described.^{37,38,99}

Cell surface rendering and cell long axis extraction

To determine germ cell shape, volume, and orientation in 3D, germ cell membranes, marked by the fluorescent protein (FP)-tagged PH domain of rat PLC1 δ ,⁴⁶ were rendered using the Cells tool in Imaris (version 9.2.1, Oxford Instruments).⁹⁶ Intensity and quality filters were applied manually, on a per gonad basis, to be as close as possible to the cell membrane marker (as visualized using the Surpass viewer in Imaris). Cell statistics (cell volume, cell position, cell ellipsoid axis orientations, cell ellipsoid axis lengths, and cell ellipticity indices) were computed in Imaris and data were exported as CSV files, which were then imported into Julia (version 1.10.4).⁹⁷ Using the centrosome tracking data (as described above), the x-y-z-t coordinates of the spindle midpoint were used to extract the corresponding cell surface renderings from the Imaris output file. All remaining cells were considered interphase cells. Interphase cells were also filtered to select tracks of at least 10 timepoints, with a mean volume greater than the smallest newly divided daughter cells and lesser than the largest mitotic cells ($75 \mu\text{m}^3 < \text{cell volume} < 250 \mu\text{m}^3$), and where cell volume was relatively stable over the 10-frame track duration (standard deviation $< 20 \mu\text{m}^3$ and mean rate of change in volume over time within $\pm 2 \mu\text{m}^3/\text{min}$). To select cells with a stable long axis, the orientation of the ellipsoid major axis at each timepoint was used to calculate the mean orientation of the long axis over time, and cells were excluded when frame-to-frame orientations deviated significantly from this mean (mean difference between measured orientations and the calculated mean orientation $> 20^\circ$) or when the standard deviation of long axis orientation exceeded 20° . For selected interphase cells and mitotic cells, cell shape was described by the ellipticity prolate index (e_{prolate}) of the fitted ellipsoid:

$$e_{\text{prolate}} = \frac{2a^2}{a^2+b^2} \cdot \left(1 - \frac{a^2+b^2}{2c^2} \right)$$

where a , b and c are the lengths of the three ellipsoid axes. For mitotic cells, the orientation of the cell long axis was defined as the mean orientation of the longest axis during 5 timepoints prior to anaphase onset; for interphase cells, the orientation of the cell long axis was defined as the mean orientation during the first 10 tracked timepoints.

Defining the gonadal D/P axis

The D/P axis was defined as previously described.³⁷ Briefly, a rectangle encompassing the distal region of the gonad arm at the center z-slice was drawn. The D/P axis was defined as the vector joining the midpoints of the short sides of the rectangle. In explants, the gonad was not necessarily oriented parallel to the image plane and the rectangle used to define the D/P axis was determined locally along a $30 \mu\text{m}$ stretch of the gonad surrounding each dividing cell, and adjusted as needed to accommodate gonads that were tilted relative to the imaging plane.

Rachis and gonad surface rendering

To render the rachis surface for measuring spindle orientation, z stack timelapse images were imported into Imaris and the rachis was delineated using the surface rendering tool. A Gaussian filter was applied with surface details set to $0.75 \mu\text{m}$ and the rendering threshold was adjusted manually, on a per gonad basis, to be as close as possible to the rachis surface (as visualized using the Surpass viewer in Imaris). A filter was then applied to keep only the largest object rendered per time point. The rendered surface was exported to Fiji as a binary hyperstack TIF and a custom macro was used to fill, in 3D, holes in the rendered surface. The processed TIF was then reimported into Imaris, and the rachis surface was re-rendered using the same parameters as before. The final rendered surface was exported as series of vertices and edges, forming a meshwork of triangles, in Virtual Reality Modeling Language format (WRL), which was converted to a CSV file using a custom Python 3 script⁹⁸ for use with MATLAB (version 2020b)⁹⁴ or imported directly to Julia. The gonad surface was rendered using the same method, except that surface details were set to $2 \mu\text{m}$ and the hole filling step was not necessary. Gonad surface renderings were generated using the FP-tagged PH domain or β -tubulin signal, both of which are expressed solely in the germ line. For quantifying changes in rachis morphology following LIN-5/NuMA depletion, the rachis surface was rendered within the distal-most $80 \mu\text{m}$ for all gonads and object measurements (number and volume) were exported prior to the first filtration step above.

Determining the orientation of the rachis or gonad surface for each cell

Rachis or gonad surface renderings were imported into MATLAB or Julia, where they were paired with centrosome tracking and/or cell surface rendering data. A patch of rachis or gonad surface meshwork triangles was extracted from the rendered surface for each cell at each timepoint, by calculating the Euclidean distance between the spindle midpoint and/or fitted ellipsoid centroid and the centroid of all surface triangles. Triangles were then sorted by distance and the sum of the area of all triangles within 0.01 μm of the spindle midpoint or ellipsoid centroid was calculated. This process was performed iteratively, increasing the distance from the spindle midpoint or ellipsoid centroid by 0.01 μm until the cumulative measured area reached at least 50 μm^2 or the distance reached 8 μm . If a 50 μm^2 net area was not reached within 8 μm , no patch was defined for that timepoint. A clustering analysis of the selected triangles' centroids was performed to exclude timepoints where non-contiguous patches were identified. The normal vector of the obtained patch (the rachis or gonad surface normal) was defined as the sum of the normal vectors for all triangles within the patch.

Measuring spindle and cell long axis orientations

The orientation of the spindle or cell long axis relative to the rachis surface was calculated as the angle between the rachis normal and the spindle vector or cell long axis in 3D as follows:

$$\phi_{\text{radians}} = \arccos\left(\frac{a \cdot b}{\|a\| * \|b\|}\right)$$

where a and b are the 2 vectors in 3D. ϕ was converted from radians to degrees. Angles greater than 90° were normalized to a 0°–90° range by taking the corresponding acute angle ($\phi = 180 - \phi$). The same calculation was performed when determining the orientation of the spindle or cell long axis to the D/P axis, or the orientation of the spindle to the gonad surface.

Spindle orientation measurements were compared to a theoretical random distribution, calculated as described previously.^{37,105} Briefly, the probability of a vector occupying a given angle around its midpoint, is proportional to the surface area of a sphere, centered on the vector midpoint, at that angle. For example, a sphere with a radius of 1, has circumference C at angle ϕ from its polar axis, as given by:

$$C = 2 \pi \sin \phi$$

Therefore, the surface area, A_ϕ , between the angle ϕ and the polar axis (0°) and its symmetrical counterpart $-\phi$ (with $0^\circ \leq \phi \leq 90^\circ$) can be calculated as:

$$A_\phi = \int_{-\phi}^{\phi} 2\pi \sin a \, da = -4\pi \cos \phi$$

The fraction f_ϕ of the total cortical surface area can then be calculated as:

$$f_\phi = \frac{-4\pi \cos \phi}{4\pi} = -\cos \phi + 1$$

The rachis normal, D/P axis or the cell long axis, were considered as the sphere's polar axis, depending on the spindle orientation being assessed.

To calculate the theoretical range of spindle orientations that would preclude spindle-rachis contact in anaphase, the average distance between the spindle midpoint and the rachis surface (here modeled as the best-fit plane to the rachis surface patch) and the average spindle half-length at the end of anaphase spindle elongation were considered as two sides of a right triangle (short side and hypotenuse, respectively) and used to calculate the angle between the spindle vector and rachis normal assuming that a line on the rachis plane formed the third side of the triangle.

To predict the range of spindle orientations to the rachis normal at anaphase onset if the only constraint were spindle orientation at NEBD, the measured angles between the spindle vector and the rachis normal from NEBD to anaphase onset for the cells analyzed in Figure 1 were used to calculate the frame-to-frame change in spindle angle, with the direction of rotation (towards or away from the rachis normal) preserved (hereafter rotation). We note that because spindle angles were reported as within 0°–90° of the rachis normal, the range of rotations used here underestimates the true extent of spindle movement. A basic simulation was then run in MATLAB in which a starting angle and a duration of mitosis (NEBD to anaphase onset) were drawn at random from all measured values, and a set of rotations, with the number determined by the duration of mitosis (one rotation per frame), were drawn at random from all measured rotations for all cells. Net rotation during mitosis was calculated by summing the set of randomly drawn rotations and the resulting angle at anaphase onset was calculated as the angle at NEBD + net rotation, with obtuse anaphase angles returned to within 0°–90° of the rachis normal, as above. The simulation was run 1000 times, and the output was used to plot the cumulative distribution of predicted anaphase angles relative to the observed distribution and the distribution of predicted net rotations versus measured net rotations.

Cortical fluorescence intensity measurements

To measure cortical fluorescence, a series of vectors were generated using the spindle midpoint (for mitotic cells) or the cell center (defined manually in Fiji by placing a point ROI at the center point of the nucleus, as identified by the exclusion of cytoplasmic fluorescence) for interphase cells. Interphase cells were selected by size ($\geq 125 \mu\text{m}^3$) and the absence of neighboring mitotic cells. For mitotic cells, cortical fluorescence was measured along the spindle vector, the gonad surface normal (generated from the gonad surface rendering, as described above) and a third vector orthogonal to both. For interphase cells, cortical fluorescence was measured along the gonad surface normal, a vector parallel to the gonadal D/P axis passing through the cell center and a third vector orthogonal to both. A series of flattened ellipsoids ($2 \mu\text{m}$ high \times $2 \mu\text{m}$ wide \times $0.5 \mu\text{m}$ deep) were propagated along each vector, every $0.25 \mu\text{m}$, for a total distance of $6 \mu\text{m}$ on either side of the spindle/cell midpoint. The orientation and position of each ellipsoid was calculated using a custom MATLAB script, imported into Fiji, and a custom macro was used to draw the corresponding 2D ROI where the ellipsoids intersected with each z-slice. The area and raw integrated density (RID) for each 2D ROI for each ellipsoid was summed and converted to a mean fluorescence intensity (FI; total RID/total area) per ellipsoid. A custom MATLAB script was then used to plot FI, relative to distance along each vector, for both the FP-tagged PH membrane marker and LIN-5:mNG. The position of the peak FI for the membrane marker was used to identify where the vector intersected with the cell cortex and the corresponding LIN-5:mNG FI value was extracted. Background (the average minimum FI along the cell orthogonal vector) was subtracted and LIN-5:mNG FI was normalized to its respective membrane signal. For mitotic cells, LIN-5:mNG measurements were made at anaphase onset (determined by centrosome tracking, as described above) and corrected for photobleaching, according to when, relative to the start of imaging, each cell entered anaphase. Briefly, a bi-exponential function was fit to the change in FI over time in a rectangle ($\sim 20 \mu\text{m} \times 100 \mu\text{m}$) drawn on a maximum intensity projection through the gonad that encompassed the mitotic zone. The reverse of this function was then applied to the measured data. For interphase cells, FI measurements were made at the first frame of the movie. For mitotic cells, the reported spindle and orthogonal vector values show the mean FI for both cortices along each vector at anaphase onset. To avoid measuring centrosome-localized LIN-5:mNG, timepoints were excluded if the distance between the centrosome and cortex was less than $1.5 \mu\text{m}$. We also excluded cells if centrosome-localized LIN-5:mNG in neighboring mitotic cells was captured by the line scan. For interphase cells, lateral measurements reflect the mean of all 4 cortices (2 D/P + 2 orthogonal cortices).

Analysis of centrosome movement and position in prophase

Centrosome tracks were generated using TrackMate, as described above, and the x-y-z coordinates for each centrosome were expressed relative to the centroid of the nucleus. The nucleus centroid was determined either by tracking nuclei in TrackMate using the histone marker or manually in TrackMate using the exclusion of cytoplasmic fluorescence (FP- and AID-tagged LIN-5 and DHC-1) to identify the nucleus. Frame-to-frame centrosome movement was assessed by assuming that centrosomes move around the surface of the nucleus and calculating the arc length as follows: $d = \phi * r$, where ϕ = the central angle between centrosome positions at adjacent timepoints and r = nuclear radius (as defined by the distance between the centrosome and the center of the nucleus).

Measuring centrosome position in interphase cells

The x-y-z coordinates of the centroid of select nuclei were used to generate a $10 \mu\text{m}$ -thick stack, oriented orthogonally to the gonadal D/P axis, and centered on each nucleus, using the “Reslice” tool in Fiji. Maximum intensity projections of the resliced stack were used to create a cross-sectional view of the gonad and a $3 \mu\text{m}$ -thick line was drawn from the center of the gonad, through the center of the nucleus towards the basal surface of the gonad, approximating the gonadal radial axis. Fluorescence intensities for both FP-tagged histone and γ -tubulin were plotted and used to define the diameter of the nucleus and the position of the centrosomes on the nucleus, along the gonadal radial axis. Centrosome position was expressed as a percent of nuclear diameter. To exclude mitotic cells, only cells where a single γ -tubulin focus was visible were analyzed.

QUANTIFICATION AND STATISTICAL ANALYSIS

Statistical analysis was performed in MATLAB or Julia. One-sample Kolmogorov-Smirnov tests (MATLAB `kstest`) with Bonferroni corrections,¹⁰⁶ as needed, were used to compare the distribution of measured angles to the theoretical random distribution. Two-sample Kolmogorov-Smirnov tests (MATLAB `kstest2`) with Bonferroni corrections, as needed, were used to compare the distribution of measured angles between two samples. Kruskal-Wallis tests with a Tukey-Kramer post hoc test (MATLAB `kruskalwallis` and `multcompare`) were used to compare multiple independent samples means. Two-tailed Student's t-tests (MATLAB `ttest2`) were used to compare two independent samples, except when comparing the duration of mitosis between cells in explants versus *in situ*, where a two-tailed Student's t-test with unequal variance was used (MATLAB `ttest2` with `Vartype = unequal`), and when comparing the rachis volume in controls vs. LIN-5 depleted conditions, where a two-sided Wilcoxon rank-sum test was used (MATLAB `ranksum`). A one-sample t test (MATLAB `ttest`) was used to test if centrosome midpoint displacement during prophase had a mean different from zero. Bartlett multiple-sample tests for equal variances (MATLAB `vartestn`) were used to compare the variance of centrosome separation in controls and LIN-5 or DHC-1 depleted conditions, followed by a two-sample F-test for equal variances (MATLAB `vartest2`) to identify which pairs were significantly different. A two-sample F-test for equal variances (MATLAB `vartest2`) was used to compare the

variance of cell volume in controls vs. LIN-5 depleted conditions. All summary statistics are provided by figure panel in [Table S3](#). Figures were assembled using Adobe Illustrator. Graphs were generated in MATLAB or Julia, saved as PDFs and imported into Illustrator to generate high resolution, vector-based graphics. All representative images were processed in Fiji (scaled to the same brightness and contrast settings, pseudo colored and cropped) and exported as RGB TIFs. Images were re-sized and/or cropped in Illustrator to fit the final figure panel.